The Potential Roles of Preexisting Airmass Boundaries on a Tornadic Supercell Observed by TORUS on 28 May 2019

KRISTEN L. AXON,[a] ADAM L. HOUSTON,[a] CONRAD L. ZIEGLER,[b,c] CHRISTOPHER C. WEISS,[d] ERIK N. RASMUSSEN,[e] MICHAEL C. CONIGLIO,[b,e] BRIAN ARGROW,[f] ERIC FREW,[f] SARA SWENSON,[f] ANTHONY E. REINHART,[c] AND MATTHEW B. WILSON[a]

[a] *Department of Earth and Atmospheric Sciences, University of Nebraska–Lincoln, Lincoln, Nebraska*
[b] *School of Meteorology, University of Oklahoma, Norman, Oklahoma*
[c] *NOAA/OAR/National Severe Storms Laboratory, Norman, Oklahoma*
[d] *Department of Geosciences, Texas Tech University, Lubbock, Texas*
[e] *NOAA/National Severe Storms Laboratory, Norman, Oklahoma*
[f] *Ann and H. J. Smead Aerospace Engineering Sciences, University of Colorado Boulder, Boulder, Colorado*

(Manuscript received 9 January 2023, in final form 18 October 2023, accepted 23 October 2023)

ABSTRACT: On 28 May 2019, a tornadic supercell, observed as part of Targeted Observation by UAS and Radars of Supercells (TORUS) produced an EF-2 tornado near Tipton, Kansas. The supercell was observed to interact with multiple preexisting airmass boundaries. These boundaries and attendant air masses were examined using unoccupied aircraft system (UAS), mobile mesonets, radiosondes, and dual-Doppler analyses derived from TORUS mobile radars. The cool-side air mass of one of these boundaries was found to have higher equivalent potential temperature and backed winds relative to the warm-side air mass; features associated with mesoscale air masses with high theta-e (MAHTEs). It is hypothesized that these characteristics may have facilitated tornadogenesis. The two additional boundaries were produced by a nearby supercell and appeared to weaken the tornadic supercell. This work represents the first time that UAS have been used to examine the impact of preexisting airmass boundaries on a supercell, and it provides insights into the influence environmental heterogeneities can have on the evolution of a supercell.

KEYWORDS: Supercells; Storm environments; In situ atmospheric observations; Unpiloted aerial systems; Microscale processes/variability

1. Introduction

a. Background

The interaction between preexisting airmass boundaries and supercells is known to support storm intensification, storm longevity, and tornadogenesis (Maddox et al. 1980; Markowski et al. 1998; Atkins et al. 1999; Johns et al. 2000; Rasmussen et al. 2000; Groenemeijer et al. 2011; Laflin and Houston 2012; Honda and Kawano 2016). Mesoscale variability within air masses that occur along synoptic fronts or with remnant thunderstorm gust fronts can be particularly favorable for tornadic supercells with conditions such as high boundary layer relative humidity and enhanced vertical and horizontal vorticity (Maddox et al. 1980). Maddox et al. (1980) developed a theoretical model of boundary layer vertical wind profiles across typical synoptic-scale airmass boundaries associated with severe weather in which a favorable zone for tornadic supercells exists along a boundary (Fig. 1a; Maddox et al. 1980). Previous research has highlighted robust associative relationships between preexisting airmass boundaries and tornadic supercells (Markowski et al. 1998; Rasmussen et al. 2000; Honda and Kawano 2016) with nearly 70% of significant tornadoes intercepted during the Verification of the Origins of Rotation in Tornadoes Experiment (VORTEX) occurring near boundaries (Markowski et al. 1998).

At mesoscales, as storms interact with airmass boundaries they encounter additional baroclinic horizontal vorticity generated from buoyancy gradients on the immediate cool side of the boundary (Markowski et al. 1998; Atkins et al. 1999; Rasmussen et al. 2000; Laflin and Houston 2012). This horizontal vorticity is considered the predominant means by which storms interacting with boundaries obtain or strengthen low-level rotation and increase the likelihood for tornadogenesis (Markowski et al. 1998; Atkins et al. 1999; Rasmussen et al. 2000; Laflin and Houston 2012).

The likelihood of tornadogenesis and the track length of tornadoes generally depend on the orientation of the boundary relative to the storm's motion. When a storm moves parallel to a boundary, tornadogenesis is more likely (Atkins et al. 1999; Magee and Davenport 2020) and longer-lived tornadoes tend to occur (Magee and Davenport 2020). It is hypothesized that storms propagating along boundaries have sustained access to the baroclinic horizontal vorticity associated with the boundary allowing for more persistent rotation to be maintained (Markowski et al. 1998). Moreover, direct augmentation of the deep convective updraft by forced ascent at the boundary can amplify low-level vertical vorticity (Laflin and Houston 2012). It is further hypothesized that storms that continue farther into the cool air mass "behind" a boundary and interact with increasingly stable air weaken as parcels become less buoyant, suppressing vertical motion over time (Markowski et al. 1998). This would explain why tornadoes are often shorter lived when the parent storm crosses the boundary instead of moving along it.

Corresponding author: Kristen Axon, kristenaxon14@gmail.com

DOI: 10.1175/MWR-D-23-0007.1

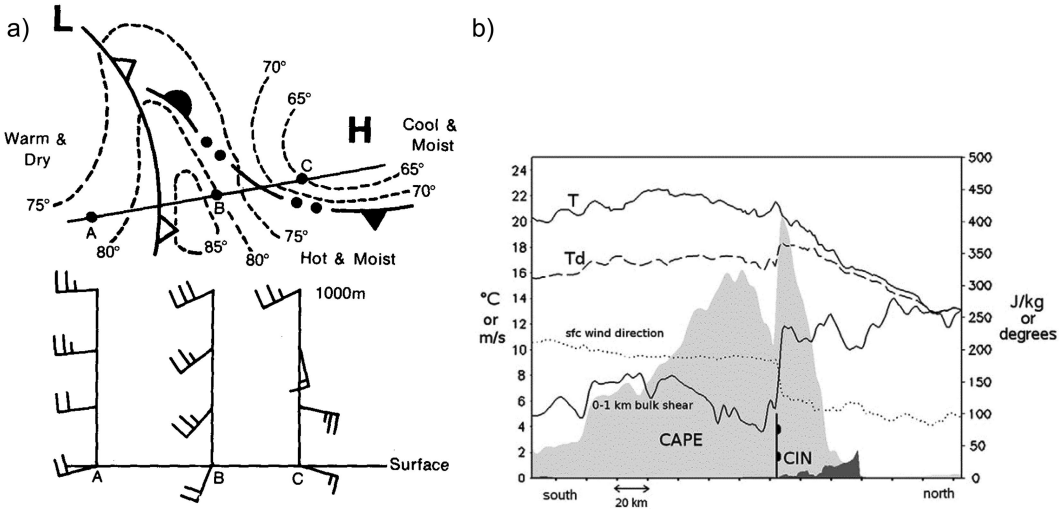

FIG. 1. (a) Schematic of the boundary layer wind profiles across boundaries typical for severe weather setups taken from Maddox et al. (1980). The region across points B (characterized as a hot and conditionally unstable air mass) and C (characterized as cool and stable thunderstorm outflow) represent a region with cyclonic vorticity, convergence, and a mixing zone that generally support rotating thunderstorms. (b) A north–south cross section from Fig. 15 in Groenemeijer et al. (2011) at 1300 UTC across a warm front. Parameters include temperature at 1000 hPa (continuous line; top; °C), dewpoint temperature (dashed line; °C), wind direction at 10 m AGL (dotted; °), 0–1-km bulk shear (continuous line; m s^{-1}), SBCAPE (light shading), and CIN (dark shading).

A mesoscale air mass with high theta-e (MAHTE; Hanft and Houston 2018) can be found in association with some preexisting airmass boundaries and may be locally favorable for storm intensification and tornadogenesis (Rasmussen et al. 2000). A MAHTE forms on the immediate cool side of boundaries and is characterized by higher low-level moisture and higher equivalent potential temperature (Θ_e) relative to the warm-side environment which can yield larger convective available potential energy (CAPE) (Rasmussen et al. 2000; Guyer and Ewald 2004; Groenemeijer et al. 2011; Hanft and Houston 2018). Geostrophic adjustment in the cool-side air mass (Maddox et al. 1980) along with baroclinic generation of horizontal vorticity can elongate hodographs away from the boundary resulting in greater low-level vertical wind shear.

As an example, on 2 June 1995 in northwest Texas during VORTEX, many supercells were observed, including those that crossed into the cool side of an outflow boundary or initiated off the boundary and remained on the cool side (Rasmussen et al. 2000). The supercells within the cool air mass developed the strongest low-level rotation, even when moving 50 km into the cool side, in comparison to supercells that occurred on the warmer side of the outflow boundary. The 2 June 1995 cool-side air mass was characterized by higher low-level moisture and enhanced CAPE, compared to the warm-side air mass (Gilmore and Wicker 2002). Another example of a MAHTE was observed on 22 June 2003 in association with an outflow boundary in southeast Nebraska (Guyer and Ewald 2004). A supercell in close proximity to this MAHTE produced F0 tornadoes and hail up to 7 in. in diameter (1 in. = 2.54 cm). Another MAHTE was observed on 28 July 2005 in association with a warm front near Birmingham, United Kingdom where three tornadoes occurred (Groenemeijer et al. 2011). In this case, the environment on the immediate cool side of the warm front had higher dewpoint temperatures relative to the warm side resulting in greater Θ_e and higher surface-based CAPE (SBCAPE) and backed surface winds resulting in greater 0–1-km bulk shear (Fig. 1b from Groenemeijer et al. 2011).

The characteristics of MAHTEs can be important for supercell development and tornadogenesis. Hanft and Houston (2018) explored the processes that lead to their initial formation by using the Advanced Research Weather Research and Forecasting (WRF-ARW) Model to simulate the development and evolution of a MAHTE that occurred on 20 June 2016 along a cold front in northwest Kansas. They determined that a MAHTE can form due to differences in the stability of air masses across a boundary which result in the differential vertical advection of moisture. The cooler side, which is initially more stable earlier in the day, becomes more resistant to mixing from daytime heating. On the warm side, drier air aloft advects down into the planetary boundary layer reducing the overall moisture content in this air mass. MAHTEs are considered meso-γ scale (Rasmussen et al. 2000; Groenemeijer et al. 2011) so current observation networks and numerical models usually lack sufficient spatial resolution to discern MAHTEs.

During the 2019 field phase of Targeted Observation by Radars and UAS of Supercells (TORUS; Houston et al. 2020b), a tornadic supercell was sampled by instrumented in situ and remote platforms on 28 May 2019 near Tipton, Kansas. Also sampled was a synoptic-scale warm front that extended across northeast Kansas into northern Missouri. Mobile mesonets measured a modest increase (2–3 K) in dewpoint on the immediate cool side when crossing this boundary. It is hypothesized that this preexisting airmass boundary (referred

to as the front henceforth) and accompanying cool air mass, with characteristics of a MAHTE, provided an optimal, but spatially limited, environment for tornadic supercells. Two other boundaries were sampled near the Tipton supercell associated with stable air masses hypothesized to be outflow boundaries from a nearby nontornadic supercell that caused the demise of an EF2 tornado and prevented more tornadoes from developing.

To gain a more detailed perspective into the air masses ahead of and behind the boundaries of this case, observations collected by unoccupied aircraft systems (UAS) operating in conjunction with mobile mesonets, mobile ground-based radar, and mobile sounding systems were examined. Previous observational studies of tornadic supercells in proximity to boundaries primarily relied on in situ observations near the surface and vertical profiles taken by radiosondes (e.g., Markowski et al. 1998; Rasmussen et al. 2000; Groenemeijer et al. 2011). Major benefits to using UAS involve their ability to target specific regions of interest and flexibility in sampling strategy. UAS can characterize the horizontal and vertical distributions of state variables across airmass boundaries in a way that is difficult or impossible using ground-based instrumentation and radiosondes (Elston et al. 2011). Since supercell evolution is a function of the storm's local environment, projects such as TORUS that sample these environments with a dense network of observations resolve local conditions well. No prior study has specifically examined the impact of a preexisting airmass boundary on a supercell using UAS observations.

b. Case overview

The synoptic environment on 28 May 2019 over northeast Kansas supported the potential for severe storms (NOAA 2019). A brief discussion focusing on the period from 1200 UTC 28 May to 0000 UTC 29 May 2019 is provided for context. Beginning at 1200 UTC, a 500-hPa trough was situated over the western United States and slowly drifted eastward. Heights fell by approximately 30 m over northeast Kansas from 1200 to 0000 UTC, but the trough remained west of the TORUS domain during the 28 May. At the same level, an upper-level jet was present on the eastern side of the trough oriented from southwest to northeast with the jet axis initially over western Kansas. By 0000 UTC, the jet had moved east northeast to a position over the central and eastern regions of the state and weakened but still had maximum wind speeds around 70 kt (1 kt $\approx$ 0.51 m s^{-1}) by 0000 UTC. The temperatures at 500 hPa decreased minimally (by $\sim$1°C) during this period but dewpoints decreased more substantially (by $\sim$25°C) indicating drying in the mid- and upper levels. At 700 hPa, the temperatures also decreased (by $\sim$2°C) while the dewpoints experienced a small increase of $\sim$2°C.

Figure 2 provides an overview of the region of interest including the EF2 tornado track and the general location of synoptic fronts. Early morning convection over central and northeastern Kansas gave way to clearing south of the zonally oriented front and residual cloud cover north of this front. A line of cumulus developed along the front around 1820 UTC indicating its location across Kansas (Fig. 3a). At 1931 UTC, a

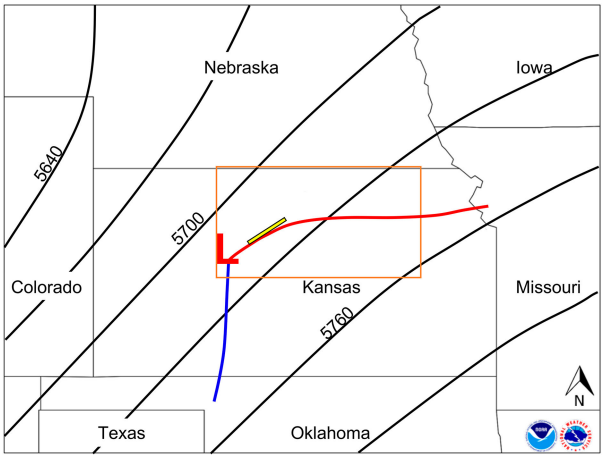

FIG. 2. Summary graphic using the Severe Storm Prediction (SPC) Interactive Local Storm Reports (SPC 2022a) from 28 May 2019. The approximate location of the EF2 tornado track associated with the Tipton supercell is the outlined yellow rectangle (NWS 2021b). Also shown is the location of the warm front (red solid curve), cold front (blue solid curve), and low pressure center (red L) at 1800 UTC according to the Weather Prediction Surface Analysis (WPC 2022). The 500-hPa geopotential height contours at 1200 UTC (Plymouth State Weather Center 2022) are the black solid curves (in m), and the orange box is the approximate domain of the satellite image in Fig. 3.

TORUS sounding (see yellow star in Fig. 3a for location) showed MLCAPE of 3746 J kg^{-1} and mixed-layer convective inhibition (MLCIN) of $-$0.87 J kg^{-1} within the warm sector (Fig. 4). The 0–6-km bulk wind differential was 52 kt, and thus conditionally supportive of supercells (Thompson et al. 2003). However, the vertical wind profile indicates weak low-level shear resulting in 0–1-km storm relative helicity (SRH) of 79 m^2 s^{-2}, which is below values typically considered conditionally supportive for tornadic supercells (Thompson et al. 2003).

Around 2018 UTC, towering cumulus began developing (Fig. 3b) and would evolve into the supercell that later produced an EF2 tornado near Tipton, Kansas (referred to as the Tipton supercell henceforth; Fig. 3b). By 2108 UTC, a second storm initiated to the northeast of the developing Tipton storm (Fig. 3c), later becoming a nontornadic supercell.[1] Both storms displayed overshooting tops around 2218 UTC (Fig. 3d) when a second TORUS sounding was launched in the far field environment (see orange star in Fig. 3d for location). The 2219 UTC sounding (Fig. 5) indicated that the 0–1-km SRH remained virtually unchanged. The environment remained supportive of supercell storm modes, but the low-level environmental shear remained small relative to values typically observed in tornadic supercell environments.

[1] The SPC preliminary storm reports for 28 May 2019 in north-central Kansas show two tornado reports associated with the nontornadic supercell (SPC 2022b). Upon surveying, the NWS Hastings, NE, found no damage to verify these two reports (M. Moritz 2023, personal communication).

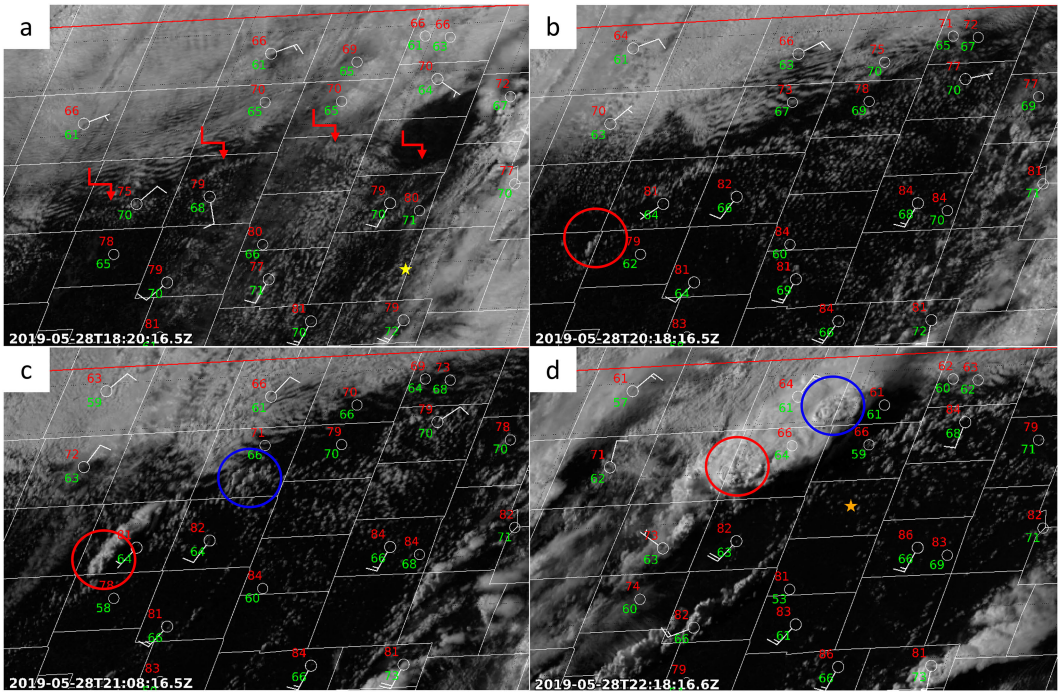

FIG. 3. *GOES-16* visible satellite imagery over north-central Kansas overlaid with Kansas mesonet surface station plots with temperature in Fahrenheit (dewpoint in Fahrenheit) in the top (bottom)-left corner in red (green) at (a) 1820, (b) 2018, (c) 2108, and (d) 2218 UTC. Wind barbs are in knots. In (a), the red arrows highlight the line of cumulus clouds developing along the front. In (b)–(d), the red circle highlights towering cumulus associated with the Tipton supercell and the blue circle highlights towering cumulus associated with the nontornadic supercell. The yellow (orange) star demarcates the location of a TORUS sounding at 1931 UTC (2219 UTC).

It is clear that the proximity TORUS soundings (within 75 km of the Tipton storm) did not fully capture the low-level environment that may have influenced the Tipton supercell. Moreover, the existing meteorological surveillance network is generally too sparse to resolve this local environment, particularly in the presence of small-scale environmental heterogeneities like those associated with airmass boundaries. The parameters deemed to best differentiate tornadic from nontornadic environments relate to boundary layer moisture and low-level winds, e.g., lifting condensation level (LCL), and low-level SRH (Thompson et al. 2003). Heterogeneities in these parameters are typical of airmass boundaries. Anticipating how a storm may evolve when interacting with environmental heterogeneities is crucial to improving warning lead times for severe hazards and reducing false alarm rates (NWS 2021a).

The purpose of this work is to characterize environmental heterogeneities associated with observed boundaries near (in both space and time) a supercell. The 28 May 2019 Tipton supercell had a relatively dense network of observations from TORUS with the unique addition of UAS providing information farther aloft on the thermodynamics and kinematics of the air masses influencing this storm. A more complete characterization of the low-level environment in relation to storm evolution is revealed with insights into the influence environmental heterogeneities can have on the evolution of a supercell.

The principal objectives of this study are as follows:

1) Characterize the thermodynamic and kinematic properties of the warm and cool air masses associated with the front and two outflow boundaries.
2) Use storm-scale analysis to infer the possible role of the different preexisting airmass boundaries on the tornadic supercell evolution.

2. Methodology

a. In situ observations

A timeline showing the operation period of each TORUS instrument used in this analysis on 28 May 2019 is presented in Fig. 6. The University of Nebraska–Lincoln (UNL) operated three Combined Mesonet and Tracker (CoMeT) vehicles (denoted CoMeT-1, CoMeT-2, and CoMeT-3; Houston et al. 2020a, 2021a,b). Similarly, the NSSL operated two dedicated mobile mesonets (Probe-1 and Probe-2, see Waugh 2020a) and two mobile mesonets equipped to launch soundings (FarField or FFld, see Waugh 2020a,b; lidar, see Smith and Coniglio 2019).

Two Robust Autonomous Aerial Vehicle-Endurant Nimble (RAAVEN) UAS were operated by the University of Colorado, Boulder (Frew et al. 2020) for this case (Fig. 7). The fixed-wing aircraft included a multi-hole probe (MHP) primarily used to derive the three-dimensional (3D) wind but also capable of measuring pressure, temperature, and relative humidity. Temperature

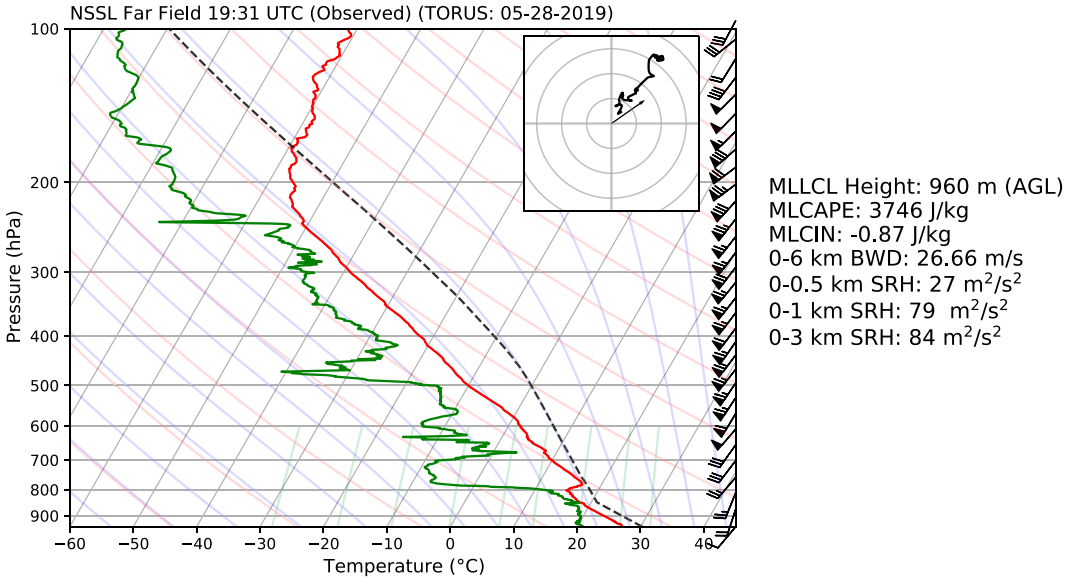

FIG. 4. 1931 UTC NSSL sounding on 28 May 2019. Hodograph rings are at 10 m s^{-1} intervals. Storm motion vector is based on the Tipton supercell's observed storm motion of 16.5 m s^{-1} from 235°. SRH values were calculated using the storm's observed motion.

and relative humidity sensors within the MHP were found to exhibit a ~11 s 63% response time which has been corrected assuming a first-order sensor, similar to the approach of Miloshevich et al. (2004). MHP temperature and humidity measurements can also be impacted by heating from full sun and evaporative cooling in rain. However, visible satellite imagery reveals considerable anvil shadowing during data collection on 28 May 2019, and radar reflectivity overlaid with the UAS locations indicates neither aircraft flew within precipitation. 3D winds were calibrated in postprocessing using the calibration procedure described by van Den Kroonenberg et al. (2008) and Wildmann et al. (2014). UAS observations used in vertical profiles were sorted by height and subsampled using the median value every 6.75 m.

RAAVEN-3 (referred to as the LF UAS) primarily executed horizontal transects while following the positions of CoMeT-1 and CoMeT-3 north/northeast of the Tipton supercell's mesocyclone while RAAVEN-4 (referred to as the NI UAS) performed vertical profiles in the near-inflow environment generally 13–30 km east of the mesocyclone. The first ascent of the NI UAS (at 2254 UTC) provided thermodynamic

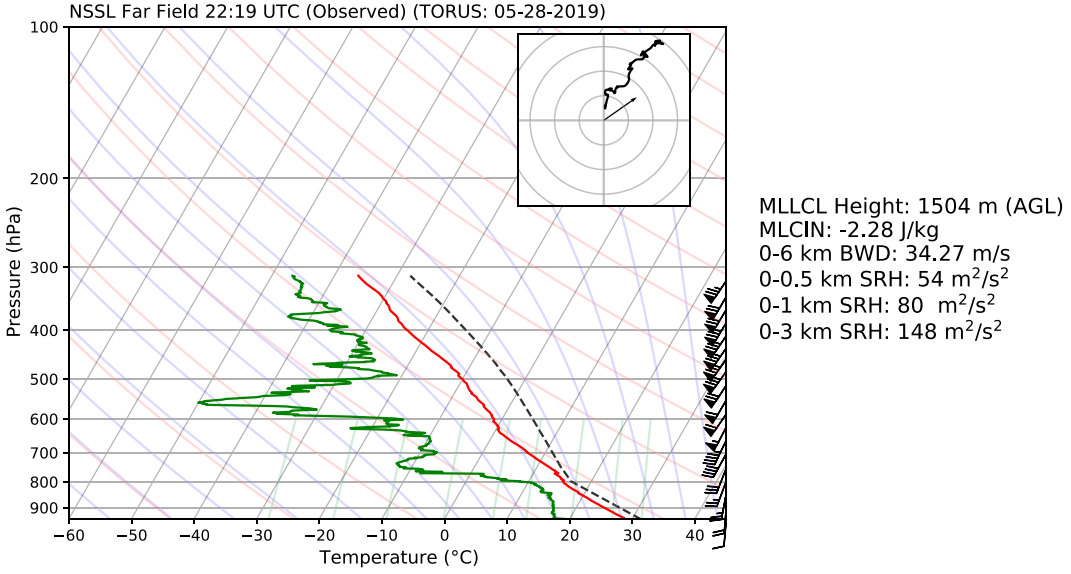

FIG. 5. As in Fig. 4, but at 2219 UTC. Note that the MLCAPE was not calculated due to data termination before the equilibrium level.

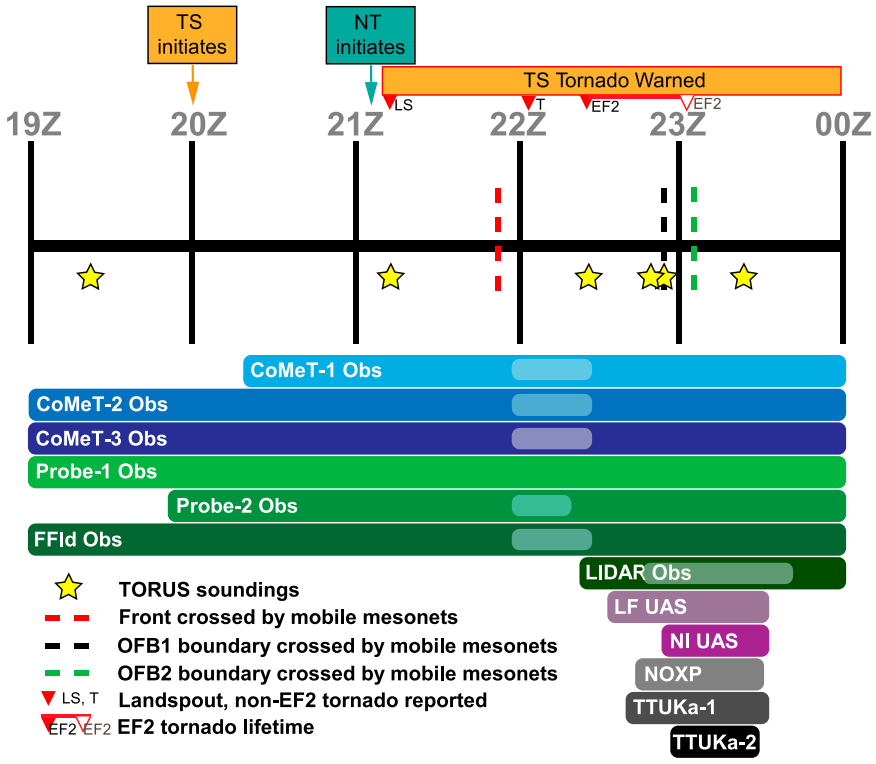

FIG. 6. Timeline of TORUS instrument operations on 28 May 2019. TS represents the Tipton (tornadic) supercell and NT represents the nontornadic supercell. The gray rounded rectangles demarcate when mobile mesonet vehicles were stationary. TORUS soundings (stars), the time when the front was crossed by mobile mesonets (red dashed line), the time when the first outflow boundary was crossed by mobile mesonets (black dashed line), the time when the second outflow boundary was crossed by mobile mesonets (green dashed line), the times when the Tipton (orange box) and nontornadic (teal box) storms initiated, the time when a landspout and non-EF2 tornado were reported (red triangles labeled LS and T, respectively), the lifetime of the EF2 tornado (filled red triangle connected to red outlined triangle labeled EF2), and the duration of the Tipton storm being tornado warned (orange box with red outline) are shown. Note that some platforms operated outside of the time period shown.

observations nearest to the surface and occurred closest in time to vertical profiles taken by the LF UAS (at 2240 UTC) and a sounding launched by the lidar mobile mesonet (at 2255 UTC). However, the wind sensor required additional adjustment time after turning on, so wind observations from the second ascent of the NI UAS (at 2300 UTC) were used in the vertical profile discussed in a later section.

b. *Mobile radars*

Three mobile radars were operated on 28 May 2019: The NOAA X-band dual-polarimetric Doppler radar (NOXP; Burgess et al. 2020) and two Ka-band radars from Texas Tech University (denoted as TTUKa-1 and TTUKa-2; Weiss and Schueth 2019) (Table 1). (Only TTUKa-2 is used for this analysis presented here.) NOXP performed deep planned-positioned-indicator (PPI) scans while the TTUKa radars implemented shallow PPI scans and range–height indicators. PPIs from NOXP and TTUKa-2 are analyzed in this study given their location and timing relative to the front, and the 0°–1° elevation tilts captured the front making these levels the focus for analysis. Radial velocities for all radars were de-aliased using the Python Atmospheric Radiation Measurement Radar Toolkit (Py-ART; Helmus and Collis 2016), and NOXP had some noise removed for gates with a normalized coherent power value below 0.3 (A. Reinhart 2022, personal communication).

For the dual-Doppler analysis, radars were gridded to the same Cartesian coordinate system in Py-ART using a single-pass Barnes objective analysis scheme (Barnes 1964) following the recommendation of Pauley and Wu (1990) where $\kappa = 1.33d$ and d is the coarsest grid spacing in the analysis domain for NOXP. This yielded a radius of influence of 776 m, which was set to be constant given the proximity of both radars to the front (~5–10 km). The grid size was 65 km × 65 km horizontally while the vertical grid levels started at 100 m above NOXP radar level since the beam height near the boundary was around this height and extended up to 6 km above ground level (AGL). This shallow vertical depth was chosen since the preexisting airmass boundaries and not the storm itself were the focus of the analysis and the associated air masses were discernible in the lowest scans of each radar (well below 6 km). NOXP

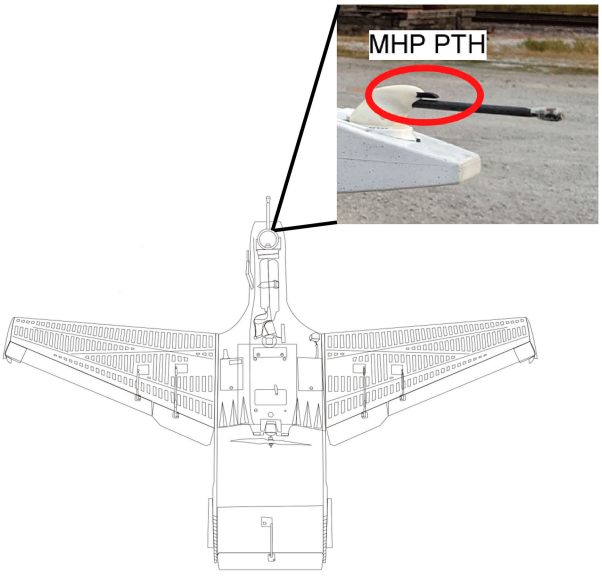

FIG. 7. RAAVEN schematic with a photo of the multi-hole probe sensor (labeled as MHP PTH in a red oval). The MHP sensor measures pressure, temperature, relative humidity, and the three-dimensional winds.

served as the grid center and grid spacing was 250 m in both the horizontal and vertical dimensions.

During operations on 28 May 2019, NOXP and TTUKa-2 had overlapping scans that included a portion of the front between 2255 and 2302 UTC. NOXP was located around 5–8 km south of the front during this period placing the beam approximately 100 m AGL relative to the surface position of the boundary while TTUKa-2 was 8–10 km north of the front also placing the beam around 100 m AGL relative to the boundary's surface position. Using the open-source Pythonic Direct Data Assimilation (PyDDA; Shapiro et al. 2009; Potvin et al. 2012; Jackson et al. 2020) package, a dual-Doppler analysis was performed to determine the two-dimensional horizontal winds across the front (the shallow elevation scans of TTUKa-2 did not permit accurate vertical motion estimates).

PyDDA uses the three-dimensional variational (3DVAR) technique to derive the 3D wind field from multiple radars by minimizing a cost function that is comprised of radial velocity observations, mass continuity, and smoothness constraints that users can customize to enhance the resultant wind field (Jackson et al. 2020). Users can also set an initial first-guess wind field using sounding data. The TORUS sounding launched at 2219 UTC (Fig. 5) was the closest to the Tipton supercell in space and time, so it was used to initialize the wind field. Constraints used for the calculations are shown in Table 2 and follow those used in Potvin et al. (2012).

TABLE 1. NOXP and TTUKa-2 radar specifications on 28 May 2019 and nominal operational characteristics during the 2019 field phase of TORUS.

Specification	NOXP	TTUKa-2
Latitude	39.3499°N	39.4957°N
Longitude	98.1163°W	98.1166°W
Altitude	458 m MSL	448 m MSL
Band	X	Ka
Half-power beamwidth	0.88°	0.33°
No. of sweeps per volume	18 (0.5°–20°)	2 (0.0°–0.5° or 0.5°–1°)
Nyquist velocity	19.14 m s^{-1}	15.05 m s^{-1}
Maximum unambiguous range	62.46 km	21.41 km

TABLE 2. PyDDA parameters.

Parameter	Setting
C_o (radar)	1
C_m (mass continuity)	30
C_x, C_y, C_z (smooth)	10^{-4}
C_v (vertical vorticity)	10^{-4}
C_b (background)	None
U_t (storm u)	13.5 m s^{-1}
V_t (storm v)	9.4 m s^{-1}
u, v, w initialization	Sounding u, sounding v, 0 m s^{-1}

While the typical beam crossing angles used in a dual-Doppler analysis range from 30° to 150° to minimize errors (Davies-Jones 1979), this case was further limited to 58°–120° to omit unrealistic winds near the edges. This resulted in a smaller domain, but the dual-Doppler lobes still contained the boundaries and the wind fields of the air masses across them (Fig. 8). The National Oceanic and Atmospheric Administration (NOAA) P-3 dual airborne tail Doppler radars were also examined for boundary identification early in the storm evolution, but clear air returns in the lowest several hundred meters AGL were insufficient to resolve the front.

c. *Storm-scale analysis*

To capture the entire evolution of the Tipton supercell, data from the KUEX WSR-88D radar, located in Blue Hills, NE, were examined in GR2Analyst. This radar is 106 km from Tipton, KS, which places the lowest elevation (0.5°) sweep at approximately 2 km above radar level (ARL) near the Tipton supercell during the TORUS operations on 28 May 2019. NWS warnings and local storm reports are included in this software providing additional details for the timing of tornadogenesis. *GOES-16* visible satellite imagery and 5-min Kansas Mesonet data (Kansas State University 2019) were also used to extrapolate the location and evolution of the synoptic-scale front based on a subjective analysis to aid in interpreting the evolution of the preexisting airmass boundaries and the supercells.

3. Results

a. *Front evolution*

Using *GOES-16* visible satellite imagery from 1815 to 2200 UTC, the location of the front was subjectively analyzed. At 1815 UTC, the cloud field exhibited a distinct line of cumulus (Cu) disclosing the location of the front at this

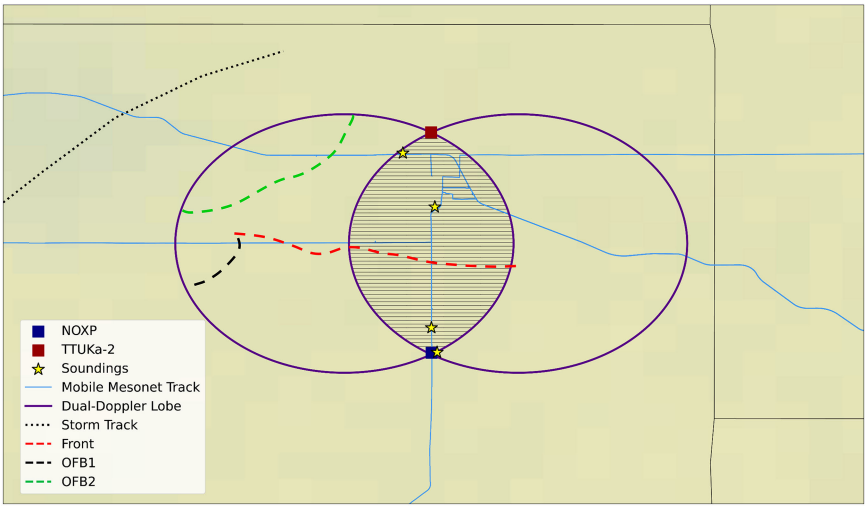

FIG. 8. Domain for the dual-Doppler analysis. NOXP and TTUKa-2 (dark blue and dark red squares, respectively), TORUS soundings (yellow stars), all mobile mesonet tracks (light blue solid lines), the 58°–120° beam crossing area of the dual-Doppler analysis domain between NOXP and TTUKa-2 (dark purple rings), storm centroid track for the Tipton supercell (black dotted curve), the front based on NOXP reflectivity observations (red dashed curve), the first outflow boundary (OFB1) based on the 2259 UTC dual-Doppler analysis (black solid curve), and the second outflow boundary (OFB2) based on the 2259 UTC dual-Doppler analysis (green dashed curve) are shown. NOXP and TTUKa-2 are 16.21 km apart. The striped region indicates where data between the radars were not used for the dual-Doppler analysis. The projection used is Plate Carrée that can distort shape, area, and scale away from the equator, which is why the lobes are elliptical.

time (see Fig. 3a for example of Cu line). Around 1900 UTC, the line of Cu became less pronounced, particularly in the more eastern section of the domain (not shown), reducing the accuracy of the subjective analysis in this area. Since mobile mesonets crossed the front at 2152 UTC, these direct observations in combination with the front's earlier movement guided the analysis for times between 1900 and 2200 UTC.

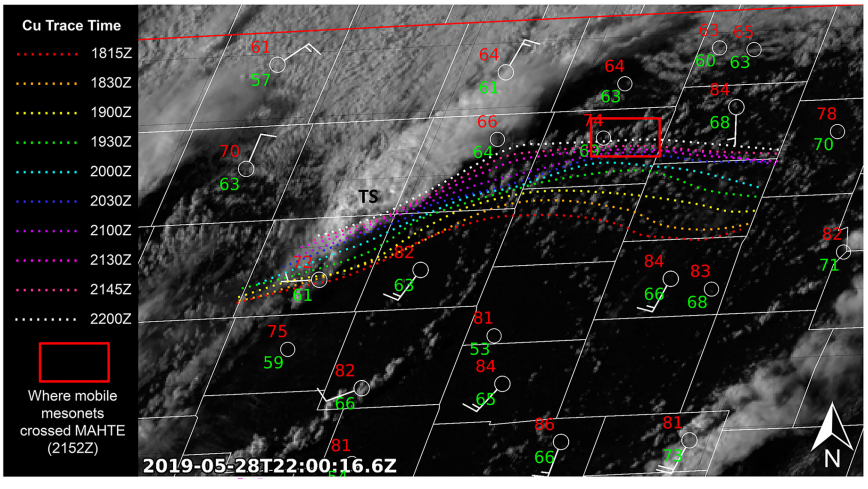

FIG. 9. *GOES-16* visible satellite imagery at 2200 UTC over north-central Kansas overlaid with dashed lines of different colors representing the subjectively determined locations of the front from 1815 to 2200 UTC. Kansas mesonet surface stations plots at 2200 UTC (white circles) are also overlaid with temperature in Fahrenheit in the top left (red), dewpoint in Fahrenheit in the bottom left (green), and wind barbs in knots. A red box gives the approximate region TORUS mobile mesonets crossed the front at 2152 UTC. Last, the boldface TS indicates the location of the Tipton supercell.

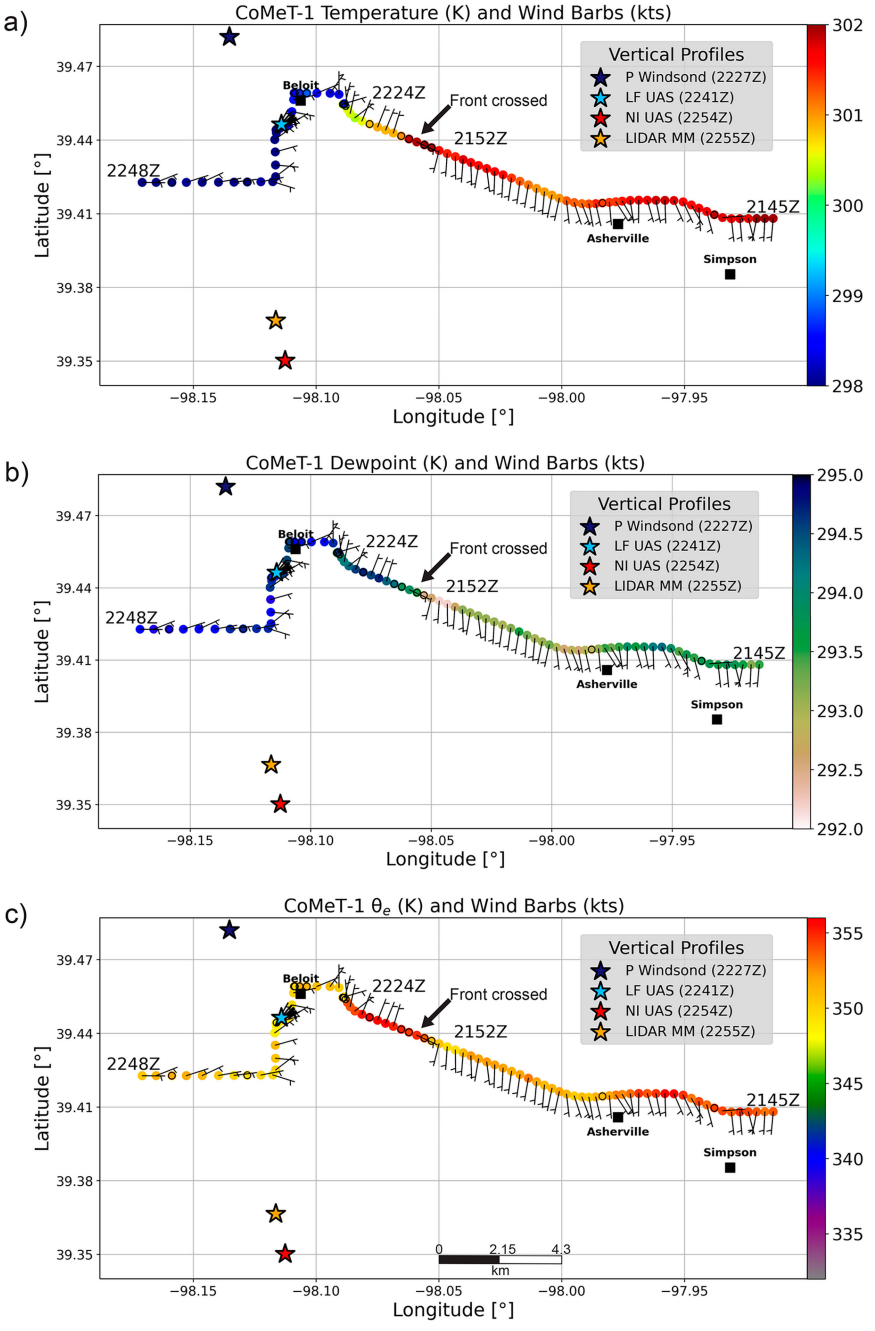

FIG. 10. CoMeT-1 wind barbs and (a) temperature, (b) dewpoint, (c) equivalent potential temperature in latitude and longitude coordinates (light gray solid lines) from 2145 to 2248 UTC (this short time period was selected to best represent the front crossing, and the mobile mesonets backtracked over the same roads later in time resulting in overlapping observations). The black arrow highlights where the front was crossed at 2152 UTC, stars represent the location of vertical profiles taken by UAS later in time, the Windsond launched by Purdue University (denoted P Windsond), and the sounding launched from the lidar mobile mesonet vehicle's location (denoted lidar MM). Towns are also included (black squares).

Figure 9 shows traces of the location of the front at 15–30-min intervals between 1815 and 2200 UTC. The general front orientation gradually transitioned to more zonally oriented farther to the east. The Tipton supercell initiated south of the front and ahead of a cold front, while the nontornadic supercell initiated on the front near the region where it became more zonally oriented (Figs. 3b–d). The front's impact on both supercells will be discussed later in this section following a discussion of the

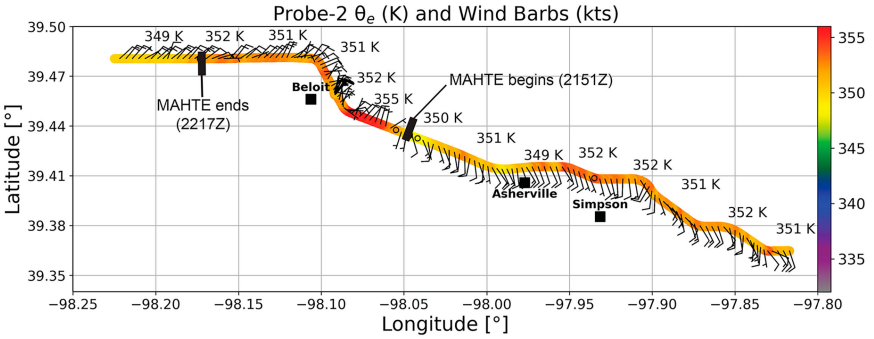

FIG. 11. Probe-2 wind barbs and equivalent potential temperature in latitude and longitude coordinates (light gray solid lines). The equivalent potential temperature is labeled at different points along the path, and the times when Probe-2 crossed into the MAHTE (2152 UTC) and out of the MAHTE (2217 UTC) are demarcated by black lines and labels. Towns are also included (black squares).

characteristics of the air mass associated with the front and other preexisting air masses.

b. *MAHTE and warm airmass characteristics*

The Kansas mesonet surface observing stations in north-central Kansas at 2200 UTC revealed the general presence of the front (Fig. 9) and indicated that dewpoints on the cool side were generally higher than on the warm side, but there was a considerable gap between stations that introduces uncertainty in these results. The dense observation network provided by TORUS was needed to better characterize these two air masses particularly close to the front and Tipton supercell.

At 2152 UTC, mobile mesonets crossed the front and observed higher moisture on the cool side and a wind shift from southerly to northeasterly (Fig. 10b). Altogether, there was a 1–3-K decrease in temperature (Fig. 10a) associated with a 2–3-K increase in dewpoint temperature (Fig. 10b) resulting in a Θ_e increase of 3–7 K (Fig. 10c) on the immediate cool side of the front. These observations support the hypothesis that the cool air mass had characteristics of a MAHTE. More specifically, CoMeT-1 observations measured a max Θ_e within the MAHTE around 357 K and the temperature and dewpoint at the max Θ_e were 301 and 295 K, respectively. Within the warm air mass immediately ahead of the front, Θ_e was observed to be around 350 K associated with a temperature of 302 K and dewpoint of 293 K. The full extent of the MAHTE along the front is unknown given sparse Kansas mesonet surface stations, but mobile mesonet observations from TORUS support its presence along the portion of the front near the Tipton and nontornadic supercells. The development of the MAHTE is not examined in this work.

To best estimate the boundary-normal width of the MAHTE, Probe-2 observations of Θ_e between 2150 and 2154 UTC were examined (Fig. 11), since this mobile mesonet continued farther north than the CoMeTs with less time parked in Beloit, Kansas. The distance between where Probe-2 crossed the front and where Θ_e decreased to below the Θ_e of the warm-side environment (~350–352 K) was calculated. Figure 11 demarcates these two points, and the approximate distance between them was estimated to be 12 km. While the initial movement of the front was to the north, observations from NOXP later in time (2249 UTC) indicated the MAHTE, and therefore front, was moving to the south. This southward movement was estimated to be around 3 km h^{-1} and resulted in an actual estimated width of 13 km. From these observations by Probe-2, the max Θ_e was 356 K and the temperature and dewpoint at the location of maximum Θ_e were 300 and 295 K, respectively. Immediately ahead of the front in the warm air mass, Θ_e was observed to be around 350 K associated with a temperature of 301 K and dewpoint of 292 K.

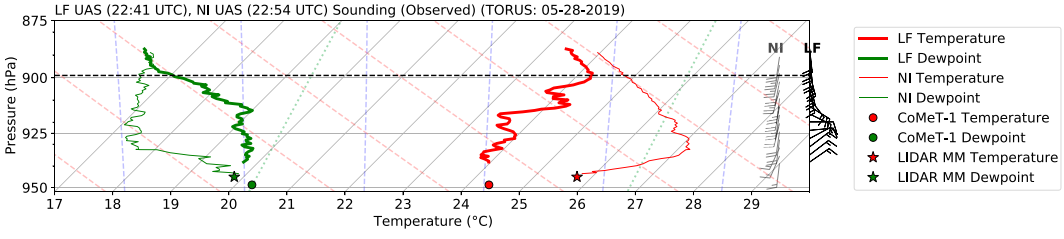

FIG. 12. 2241 UTC (2254/2300 UTC) LF UAS (NI UAS) sounding on 28 May 2019. The black (gray) wind barbs were observed by the LF UAS (NI UAS). The black dashed line denotes the top of the MAHTE. CoMeT-1 and lidar MM surface observations are denoted by circles and stars, respectively, to compare the UAS observations to the nearest surface observations. LF UAS and CoMeT-1 observations are from north of the surface position of the front and the NI UAS and lidar MM are from south of the front.

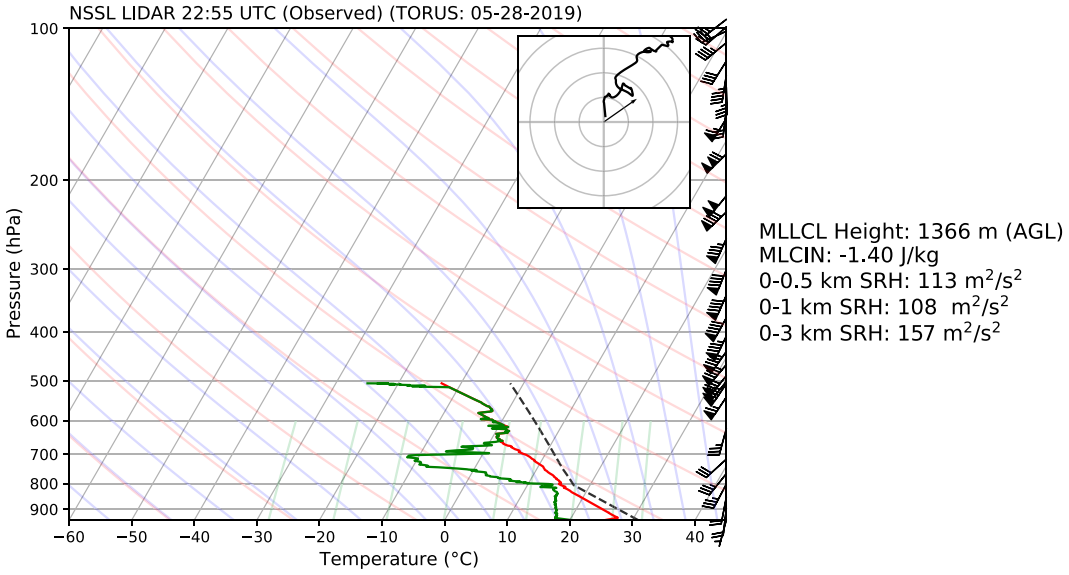

FIG. 13. 2255 UTC NSSL sounding on 28 May 2019. Hodograph rings are at 10 m s^{-1} intervals. Storm motion vector is based on the Tipton supercell's observed storm motion of 16.5 m s^{-1} from 235°. Note that the MLCAPE was not calculated due to data termination before the equilibrium level. This profile sampled the air mass south of the front.

To further investigate the MAHTE and air mass on the warm side of the front, observations collected by UAS were examined. The LF UAS and NI UAS were launched within 14 min of each other (2241 and 2254 UTC, respectively, with NI UAS winds provided from a second ascent at 2300 UTC) and obtained vertical profiles of the MAHTE and warm air mass, respectively (Fig. 12). Near the surface, there is a strong inversion in the warm air mass seen in both the temperature and dewpoint profiles (Fig. 12). This inversion suggests there was a decoupling of the near-surface atmosphere from the atmosphere aloft which is likely attributable to anvil shading (Frame and Markowski 2010; Nowotarski and Markowski 2016). This inversion can be seen in a TORUS sounding launched in the warm sector ~2 km north of the NI UAS (Fig. 10) at 2255 UTC (Fig. 13). Above this inversion, conditions are closer to what is expected for a MAHTE with cooler temperatures and higher moisture relative to the warm air mass (Fig. 12). Within the MAHTE, two inversions were evident up to 900 hPa before temperatures began decreasing at a similar rate to the warm air mass. The top of the second inversion is considered the height of the MAHTE and was around 840 m MSL (mean sea level; ~400 m AGL). Several meters above the MAHTE, the dewpoint decreased to the same value as the warm air mass also signifying the vertical depth of the MAHTE.

The NI UAS in the warm air mass observed southerly winds in the low levels that increased in speed with height (Fig. 12). The MAHTE also exhibited increasing speeds with height but had backed winds relative to the warm airmass profile in the lowest levels that transitioned to southerly above the MAHTE (Fig. 12) resulting in greater vertical wind shear in this air mass. These results align with the model of boundary layer vertical wind profiles expected across boundaries associated with tornadic supercells (Maddox et al. 1980, Fig. 1a). While this model was developed for meso-α-scale to synoptic-scale flow patterns, they compare well to the UAS observations measuring meso-γ-scale winds.

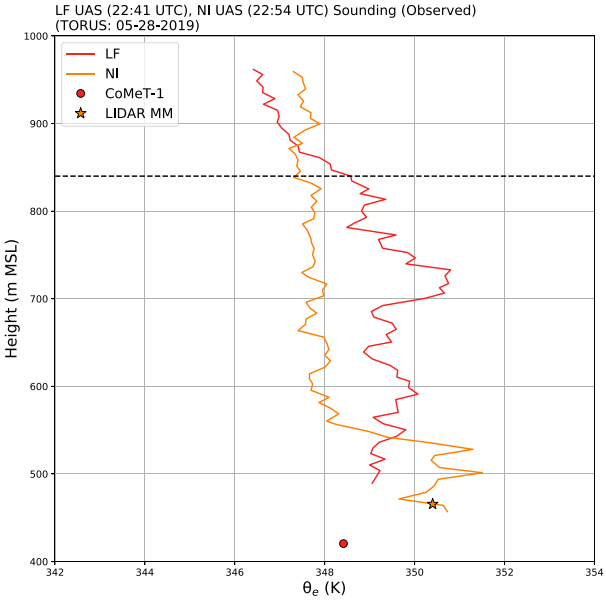

FIG. 14. 2241 UTC (2254 UTC) LF UAS (NI UAS) vertical profile of equivalent potential temperature. The black dashed line denotes the estimated top of the MAHTE. CoMeT-1 and lidar MM surface observations are denoted by a red circle and orange star, respectively, to compare the UAS observations to the nearest surface observation. Recall that the LF UAS and CoMeT-1 are on the cool side of the front and the NI UAS and lidar MM are on the warm side of the front.

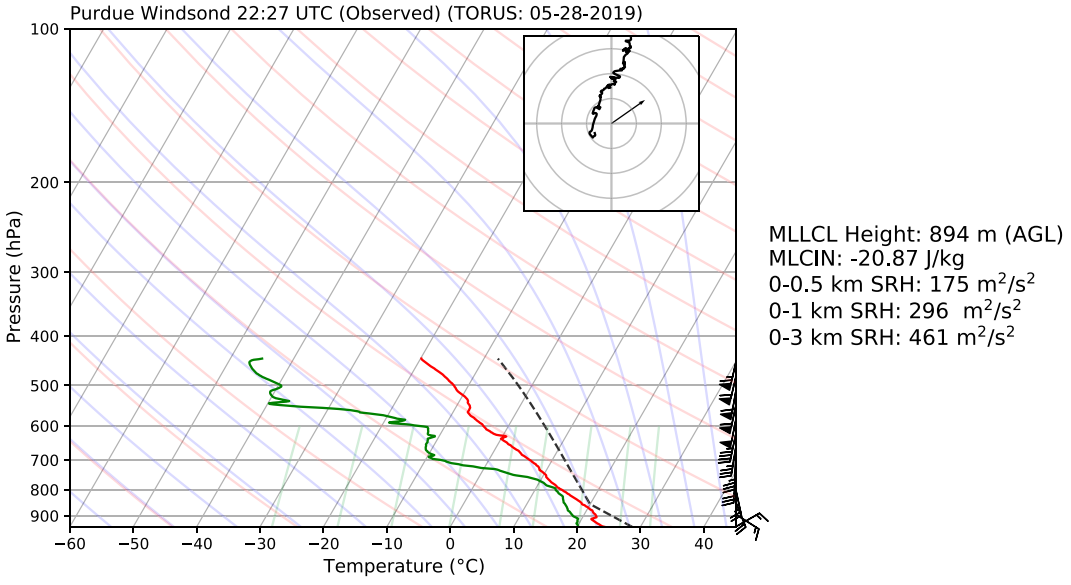

FIG. 15. As in Fig. 13, but at 2227 UTC from a Purdue University Windsond sounding.

Looking at vertical profiles of Θ_e in both air masses, the hypothesis that the cooler air mass was a MAHTE is supported above the near-surface inversion (Fig. 14), but near the surface, Θ_e was higher within the warm sector air mass until around 540 m MSL (120 m AGL). Aloft, Θ_e was 1–3 K greater throughout the vertical depth of the MAHTE relative to the warm air mass. There was also a "spike" in Θ_e of 2 K from around 700–750 m MSL (Fig. 14) that corresponded to a brief increase in dewpoint at that same level (Fig. 12). Hanft and Houston (2018) found a region of higher Θ_e in their simulated MAHTE that extended from the surface rearward into the cooler air aloft, and it is possible the LF UAS transited a similar feature in this case.

These results highlight the challenge in capturing small-scale environmental changes and the importance of observations above the surface for characterizing air masses, especially when near-surface changes occur. For this case, by the time the UAS were launched, the surface conditions no longer indicated a MAHTE was present, but above the surface, the signal remained evident.

In an effort to assess the proclivity of the MAHTE to conditionally support supercells and tornadoes, the two vertical profiles collected by UAS, which represented only the lowest ~600 m of the atmosphere, were combined with full environmental profile data. The sounding released nearest in space and time to the UAS launches occurred at 2219 UTC (Fig. 5). This sounding was launched 43 km (33 km) south of where the LF UAS (NI UAS) was launched and within the far field environment of the warm sector. Since this profile is not complete, the upper-level environment observed by an earlier sounding at 1931 UTC (Fig. 4) was combined with the 2219 UTC profile above 9275 m MSL. The LF UAS and NI UAS profiles were embedded at the bottom of the sounding and up to 969 m MSL and 965 m MSL, respectively. In addition to these modified soundings, a Windsond sounding, launched by Purdue University at 2227 UTC (D. Dawson 2021, personal communication) 4 km north of the LF UAS, provides a profile farther into the MAHTE (Fig. 10 for position of the launch and Fig. 15 for the vertical profile). Table 3 shows all sounding derived variables between the warm air mass and MAHTE from different

TABLE 3. Sounding derived variables for the warm air mass (2219/1931 UTC, 2255 UTC, and NI UAS 1 2219/1931 UTC soundings) and MAHTE/cool air mass (LF UAS + 2219/1931 UTC and 2227 UTC P Windsond soundings).

Sounding variable	2219/1931 UTC	2255 UTC	NI UAS + 2219/1931 UTC	LF UAS + 2219/1931 UTC	2227 UTC P Windsond
MLCL height (m AGL)	1504	1366	1419	1260	894
MLCAPE (J kg^{-1})	2686	—	2768	2745	—
MLCIN (J kg^{-1})	−2.28	−1.40	−5.14	−23.18	−20.87
0–1-km bulk shear (m s^{-1})	6.7	8.2	6.3	19.5	14.9
0–3-km bulk shear (m s^{-1})	18	12.9	18	31.4	24.7
0–6-km bulk shear (m s^{-1})	34.5	—	32.9	46.8	38.6
0–0.5-km SRH (m^2 s^{-2})	54	113	60	278	175
0–1-km SRH (m^2 s^{-2})	80	108	84	302	296
0–3-km SRH (m^2 s^{-2})	148	157	155	373	461

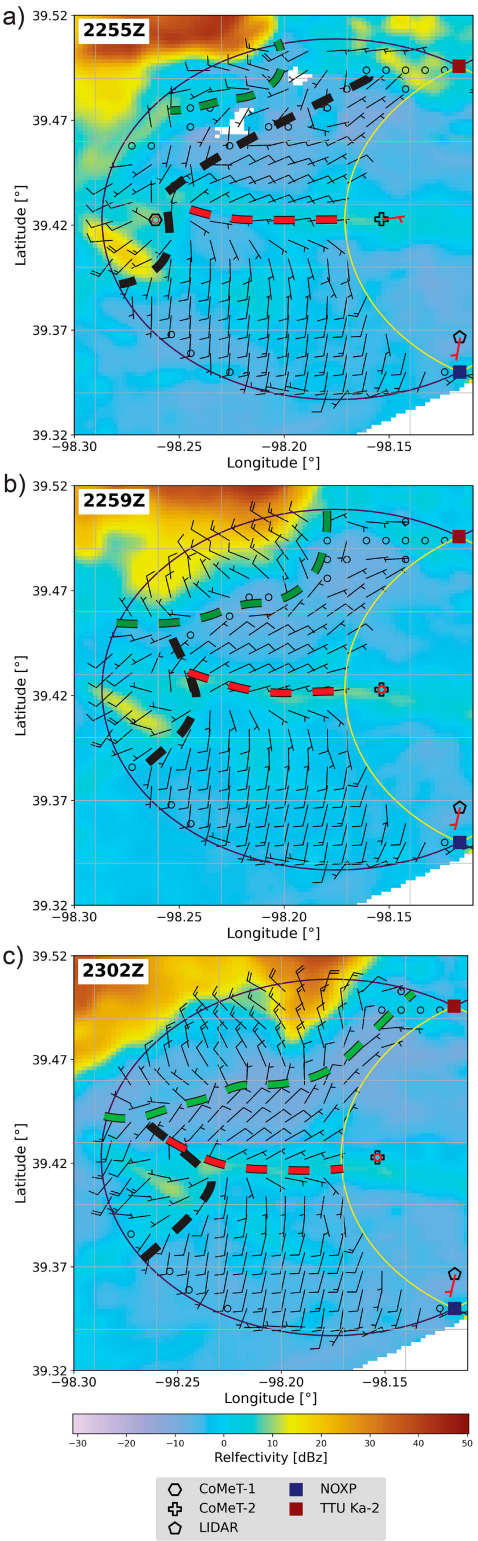

FIG. 16. Dual-Doppler analysis using NOXP and TTUKa-2 at (a) 2255, (b) 2259, and (c) 2302 UTC. NOXP and TTUKa-2 scans are from 0° to 1° with the analysis height at 100 m AGL. Overlaid are surface wind observations from mobile mesonets (red wind shaft and barbs; a circle indicates calm winds), a dashed red curve to demarcate the front, a dashed black curve to demarcate the first outflow from the nontornadic supercell, and a dashed green curve to demarcate a second outflow boundary from the nontornadic supercell. Note that the boundaries extend beyond what is annotated and by 2259 UTC, CoMeT-1 had traveled west of the domain.

sounding profiles in space and time. All sounding derived variables in this study were calculated using SHARPpy (Blumberg et al. 2017).

It is unknown if the conditions above 300 hPa in the 1931 UTC sounding represent the conditions in this layer at 2219 UTC. It is evident that the midtroposphere evolved over this time: the 2219 UTC sounding is dryer in the 700–500-hPa layer and 2–4 K cooler in the 800–500-hPa layer. Moreover, the nearest National Weather Service sounding site to Tipton, Kansas, and at a similar latitude (Topeka, Kansas, which is nearly 300 km away) featured upper-tropospheric moistening from 1800 UTC 28 May to 0000 UTC 29 May 2019 (not shown). However, the 1931 (Fig. 4) and 2219 UTC (Fig. 5) soundings are supportive of a supercell storm mode based on the 0–6-km bulk wind differentials. Moreover, the focus of this work is comparing the low-level environments of the MATHE and warm air mass and by embedding the UAS observations into the same sounding, changes between the near-surface environments are emphasized. The table of sounding variables is for general comparison purposes with the most important comparisons being made between the combined soundings.

Comparing the UAS embedded soundings, the MAHTE had an LCL height ~160 m lower than the warm-airmass environment. The MLCAPE was similar between the air masses. Both the bulk shear and SRH at all levels were greater in the MAHTE than the warm air mass (all SRH values are based on the Tipton supercell's observed storm motion of ~16.5 m s^{-1} from 235°). These results are similar to those in Groenemeijer et al. (2011) (Fig. 1b).

Overall, both the warm sector environment and the MAHTE had environments supportive of supercells. However, the greater low level SRH within the MAHTE would theoretically promote a stronger and more organized updraft. This, in combination with a lower LCL, suggests that the MAHTE may have been more likely to support tornadogenesis. On the other hand, the nontornadic supercell, which formed within the MAHTE, was never observed to produce strong rotation at the surface. This is potentially due to the MAHTE having higher CIN than the warm air mass. Whether or not tornadogenesis would have been less likely if the MAHTE did not form is not a question this work can answer, but a deeper investigation into the role the boundary may have played is carried out using mobile research radars and a dual-Doppler analysis.

A dual-Doppler analysis was performed using TTUKa-2 and NOXP data from 2255 to 2302 UTC, to investigate the 2D winds associated with the airmass boundaries of this event. Figure 16 shows the analysis at 2255, 2259, and 2302 UTC at 100 m AGL of the wind field east of the Tipton supercell. In situ wind observations from mobile mesonets within or near the dual-Doppler domain are included for comparison.

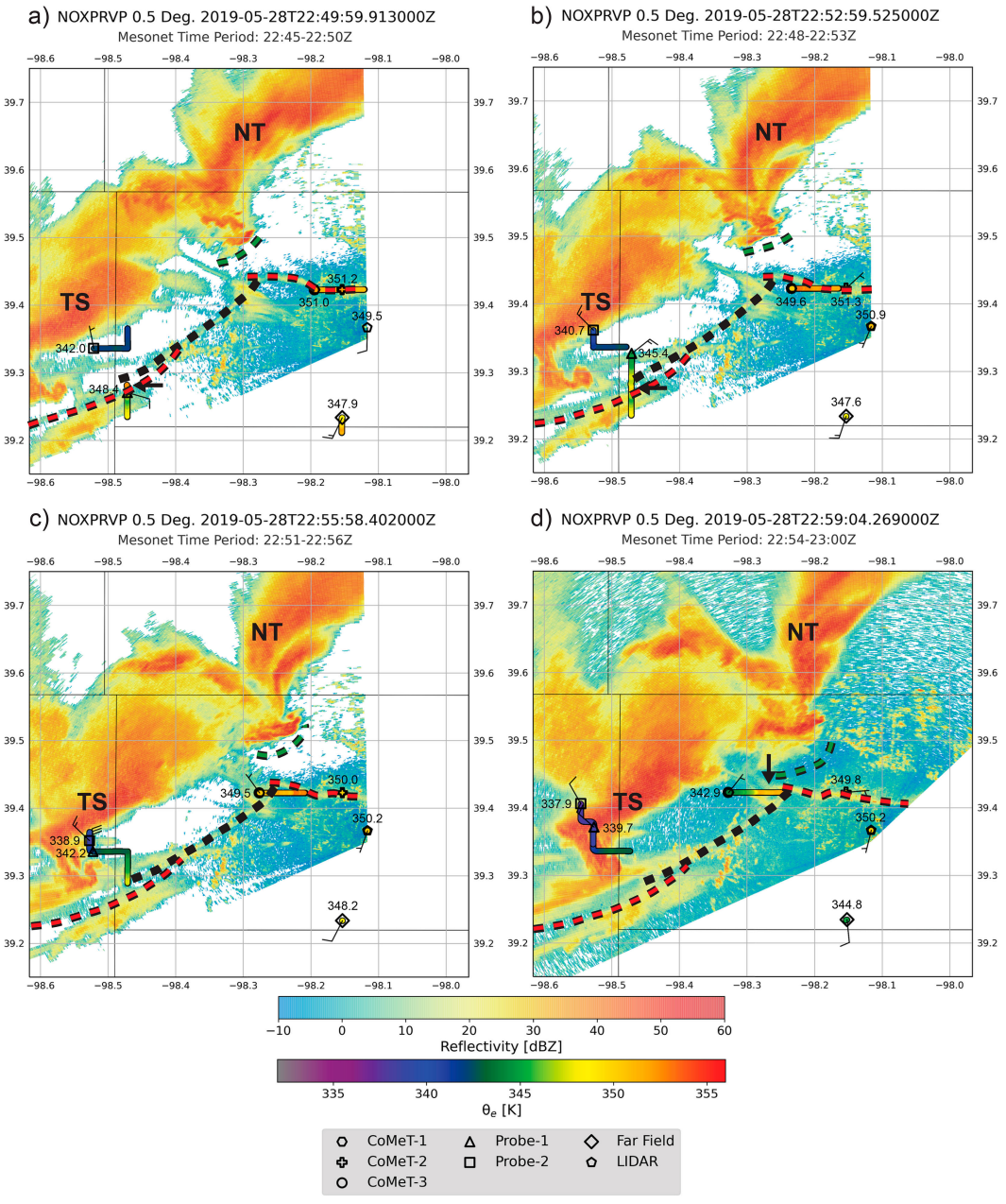

FIG. 17. NOXP reflectivity between 2250 and 2259 UTC overlaid with 5 min of mobile mesonet observations of equivalent potential temperature and wind barbs for the last observation in the 5-min period. Number labels represent the equivalent potential temperature value for the last observation in the 5-min period. The front [first outflow boundary (OFB1)] is annotated by a red (black) dashed curve. Black arrows in (a), (b), and (d) highlight important thermodynamic changes ahead of and within the air mass behind the outflow boundary. The solid gray lines are associated with the latitude and longitude points, and the thin solid black lines are county lines.

At 2255 UTC (Fig. 16a), winds within the warm sector were southerly and around 10 kt, which compared well with Kansas mesonet observations south of the front. The NSSL far-field vehicle also observed southerly surface winds around 5 kt in the warm sector just outside of the dual-Doppler lobes. Farther north, near the front, winds turned cyclonically and weakened. Within the MAHTE, winds were east-northeasterly around 5–10 kt. CoMeT-2, located just east of the analysis domain and immediately behind the front, also observed easterly to north-easterly winds around 5 kt at this time (Fig. 16a).

c. *Other preexisting airmass boundaries*

The horizontal wind pattern described above remained persistent for both the warm sector environment south of the

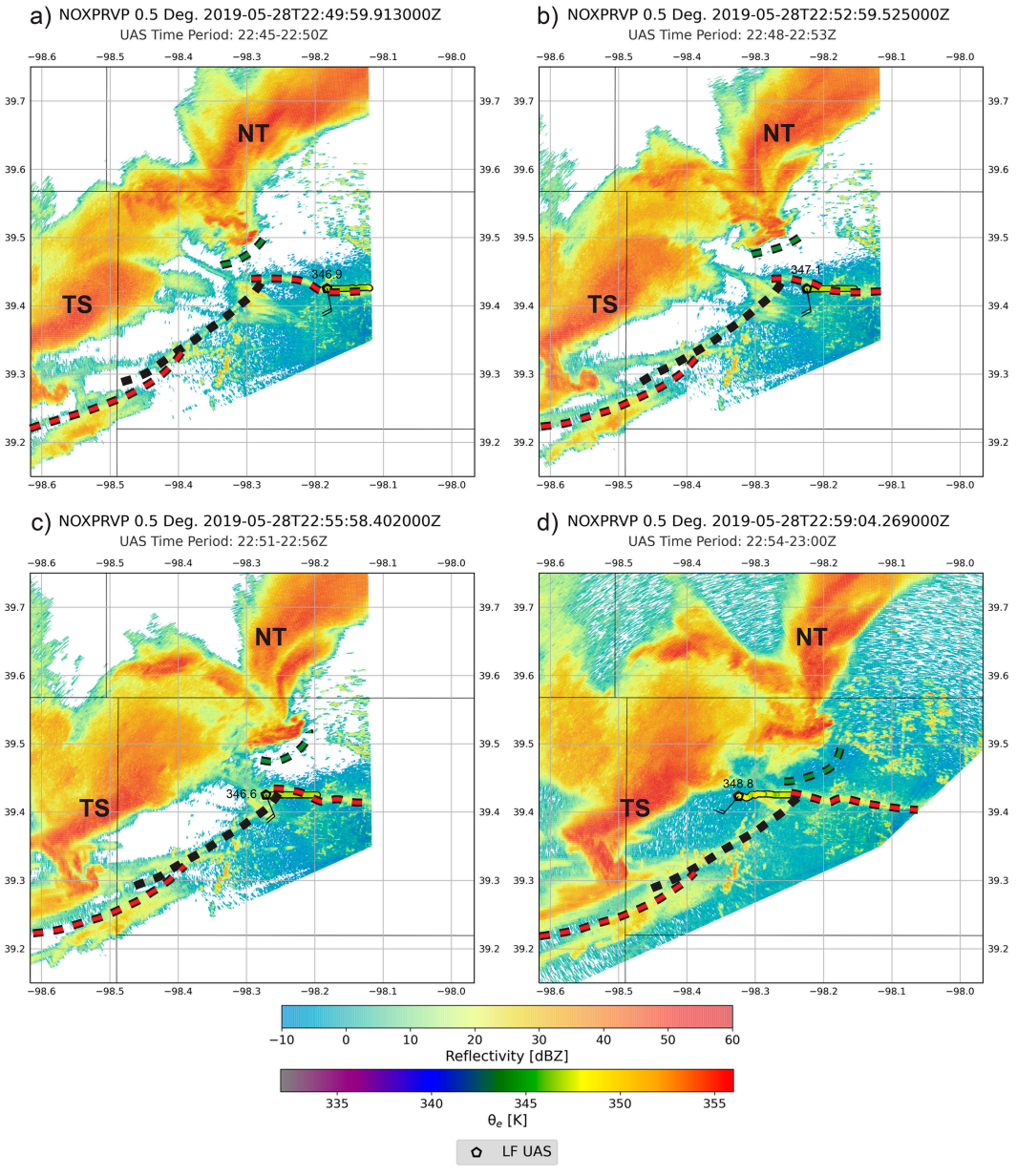

FIG. 18. As in Fig. 17, but with the LF UAS equivalent potential temperature and wind barbs plotted around 550 m AGL.

front and the MAHTE immediately north of it at 2259 (Fig. 16b) and 2302 UTC (Fig. 16c). However, other areas within the wind field showed distinct wind shifts that became more apparent in later analysis times. In the western portion of the dual-Doppler lobes, there is a region of southwesterly winds (Fig. 16a). These southwesterly winds become more evident at 2259 (Fig. 16b) and 2302 UTC (Fig. 16c) as this air mass and associated boundary pushed eastward. Closer to the surface, in situ observations from CoMeT-1 showed calm to very light northwesterly winds immediately behind this secondary boundary around 2255 UTC (Figs. 16a and 17c) which shifted to light northeasterly 2–3 km behind it (Fig. 17d). Aloft, the LF UAS observed a change in winds from south-southeasterly around 15–20 kt above the MAHTE at ~975 m MSL (~550 m AGL, Figs. 12 and 18a) to southwesterly as it passed over the secondary boundary (Figs. 18c,d).

The hypothesis for the origin of this boundary is that it was an outflow boundary from the nontornadic supercell. Probe-1, CoMeT-1, CoMeT-3, and the LF UAS all crossed the outflow boundary (henceforth denoted OFB1) but at varying locations. Probe-1 crossed the OFB1 farther south than the other platforms and closer to the Tipton supercell's mesocyclone (Fig. 17b). Both CoMeTs and the LF UAS transected OFB1 near where it intersected with the front (Figs. 17c,d; Figs. 18c,d

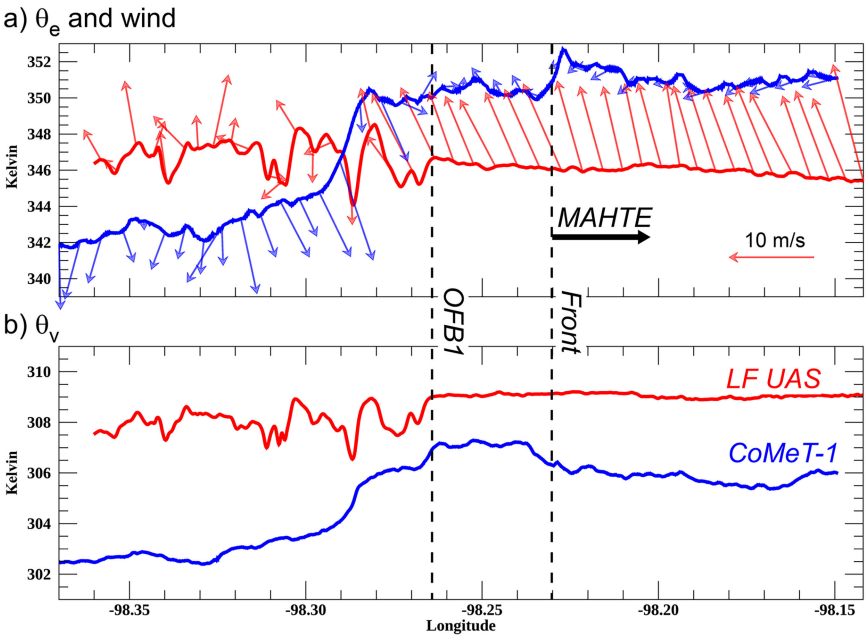

FIG. 19. CoMeT-1 (blue) and LF UAS (red) at 550 m AGL tracks of (a) equivalent potential temperature and wind vectors and (b) virtual potential temperature (Θ_v) based on longitude. Both are moving to the west, initially within the MAHTE, and then cross the front (black dashed line labeled Front) and then cross the first outflow boundary (black dashed line labeled OFB1).

and 19). All mobile mesonets observed a decrease in Θ_e of ~4 K around 2–3 km after passing the reflectivity fine line. Immediately behind OFB1, a corridor of Θ_e around 350 K was present before Θ_e decreased to 344 K (see black arrow in Fig. 17d and the nearly constant Θ_e west of OFB1 in Fig. 19a). CoMeT-1 observed northwesterly winds in the narrow region of higher Θ_e (Figs. 17c and 19a) and as Θ_e decreased to 344 K, winds shifted to a northeasterly direction (Figs. 17d and 19a).

Since the LF UAS was vertically stacked with CoMeT-1 and CoMeT-3 at this time, observations aloft were also obtained (Figs. 18 and 19). The Θ_e did not noticeably change aloft as the LF UAS passed over the near-surface position of OFB1, but the winds shifted from southerly to southwesterly farther rearward providing a kinematic indication that the UAS passed over OFB1. The virtual potential temperature (Θ_v) was also analyzed (Fig. 19b) and maintained a steady value of ~309 K until the LF UAS crossed OFB1 and then became variable but did not decrease considerably from observations over the MAHTE. The variability in Θ_e, Θ_v, and winds after the LF UAS passed over the OFB1 is likely a manifestation of turbulence expected to exist above storm outflow.

Probe-1 observations indicate a narrow region of higher Θ_e immediately between OFB1 and the front (see black arrow in Figs. 17a,b and region labeled "MAHTE" in Fig. 20a). Θ_v decreased north of the front (Fig. 20b). It is thought that the outflow boundary was trailing the front ahead of the Tipton supercell and the small region of higher Θ_e before the outflow boundary is remnants of the MAHTE behind the front.

In summary, in situ observations at the surface showed a ~8 K (~3 K) decrease in Θ_e (Θ_v) (full deficit amount as mobile mesonets continued farther into the first outflow air mass) associated with wind shifts typical of outflow boundaries and a distinct fine line in NOXP reflectivity observations. The narrow region of nearly constant Θ_e directly behind the outflow boundary where CoMeT-1 crossed was possibly a mixing zone between the outflow air mass and MAHTE and/or warm sector air mass as the more stable air overtook part of the front that was ahead of the Tipton supercell. Farther to the south, OFB1 likely was still trailing the front and had not yet overtaken the part of the MAHTE in this region. OFB1 in NOXP could be the front that has been modified by the outflow boundary, but the available observations most likely support the hypothesis described previously. Observations aloft indicated no systematic thermodynamic changes over the OFB1 air mass.

In the northwest portions of the dual-Doppler lobes (Fig. 16a), northwesterly winds were observed immediately south of the presumptive rear-flank downdraft (RFD) of the nontornadic supercell. At 2259 (Fig. 16b) and 2302 UTC (Fig. 16c), the air mass associated with these northwesterly winds moved southeast indicating a third airmass boundary near the Tipton supercell. Based on the northwesterly wind direction in this air mass and its location relative to the nontornadic supercell's RFD, it is presumed to be a second surge of outflow (OFB2) from the nontornadic supercell. Examining in situ data from mobile mesonets CoMeT-1, CoMeT-2, CoMeT-3, and the LF UAS at ~270 m AGL between 2310 and 2319 UTC (Figs. 21 and 22), a considerable drop in Θ_e around 10–12 K was observed indicating a very stable air mass was present. The front also deformed by 2319 UTC (Fig. 21d) as the strong outflow merged with it. It is likely that this stable

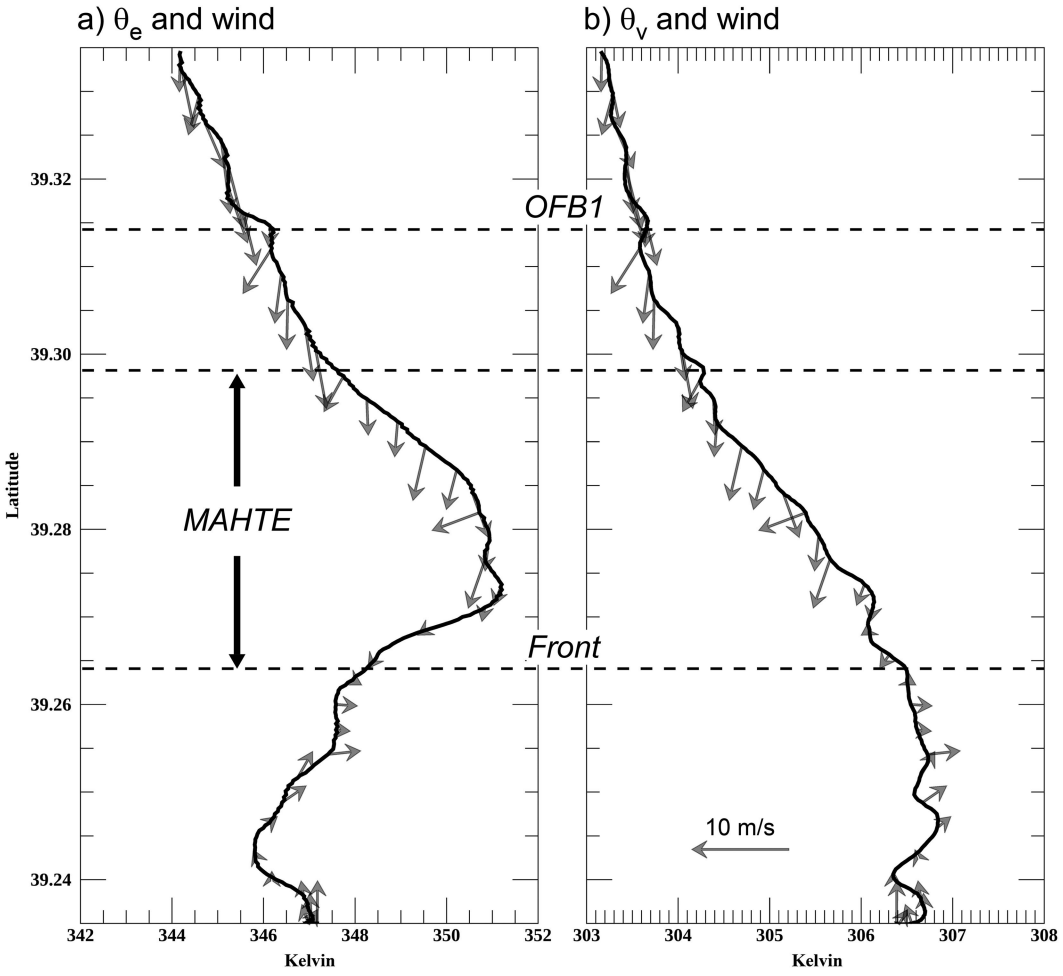

FIG. 20. Probe-1 track of (a) equivalent potential temperature and wind vectors and (b) virtual potential temperature and wind vectors based on latitude. This is from 2242 to 2248 UTC with Probe-1 moving south and crossing the outflow boundary (black dashed line labeled OFB1) into the MAHTE air mass and then crossing the front (black dashed line labeled Front) into the warm sector air mass.

outflow air mass prevented the Tipton supercell from producing more tornadoes after the demise of the EF2 tornado. Section 4d will discuss the evolution of the Tipton supercell relative to the different outflow boundaries.

d. Boundary interactions and storm evolution

To infer relationships between the different preexisting airmass boundaries and the Tipton and nontornadic supercells, an analysis of the subjective location of the boundaries relative to KUEX WSR-88D observations of the two storms was performed. Boundary positions are based on analysis described previously. Beginning at 2102 UTC (Fig. 23a), the Tipton storm was still south of the front (recall it initiated south of the front, likely ahead of a cold front) and producing moderate precipitation (40 dBZ) which intensified by 2131 UTC (Fig. 23c) as the storm moved northeast. The first tornado warning was issued around this time prompted by a landspout report. As a southwest–northeast-oriented boundary with northeast winds in the cool air and generally southerly winds in the warm air, the front was likely coincident with vertical vorticity. As such, it is possible that the occurrence of a landspout around 2131 UTC indicated that the storm was interacting with the front near this time. There is also indication of the nontornadic storm developing to the northeast of the Tipton storm where a small region of 30+ dBZ is apparent immediately north of where the front was located (Fig. 23c). By 2159 UTC , the Tipton storm showed signs of becoming supercellular with cyclonic rotation indicated in the velocity data at multiple elevation angles (Figs. 23e,f; multiple scan heights not shown). (By this time, mobile mesonets had crossed the front into the MAHTE ~105 km to the northeast of the Tipton storm.) A tornado was also reported on the Tipton supercell not long after at 2204 UTC (Fig. 6), but it was not the EF2 tornado which formed 20 min later. The nontornadic storm did not show signs of rotation (supercell storm mode) in the velocity data until ~2215 UTC. Both storms continued to move northeast, and the EF2 tornado associated with the Tipton supercell formed near Waldo, Kansas, around 2223 UTC (NWS 2021b).

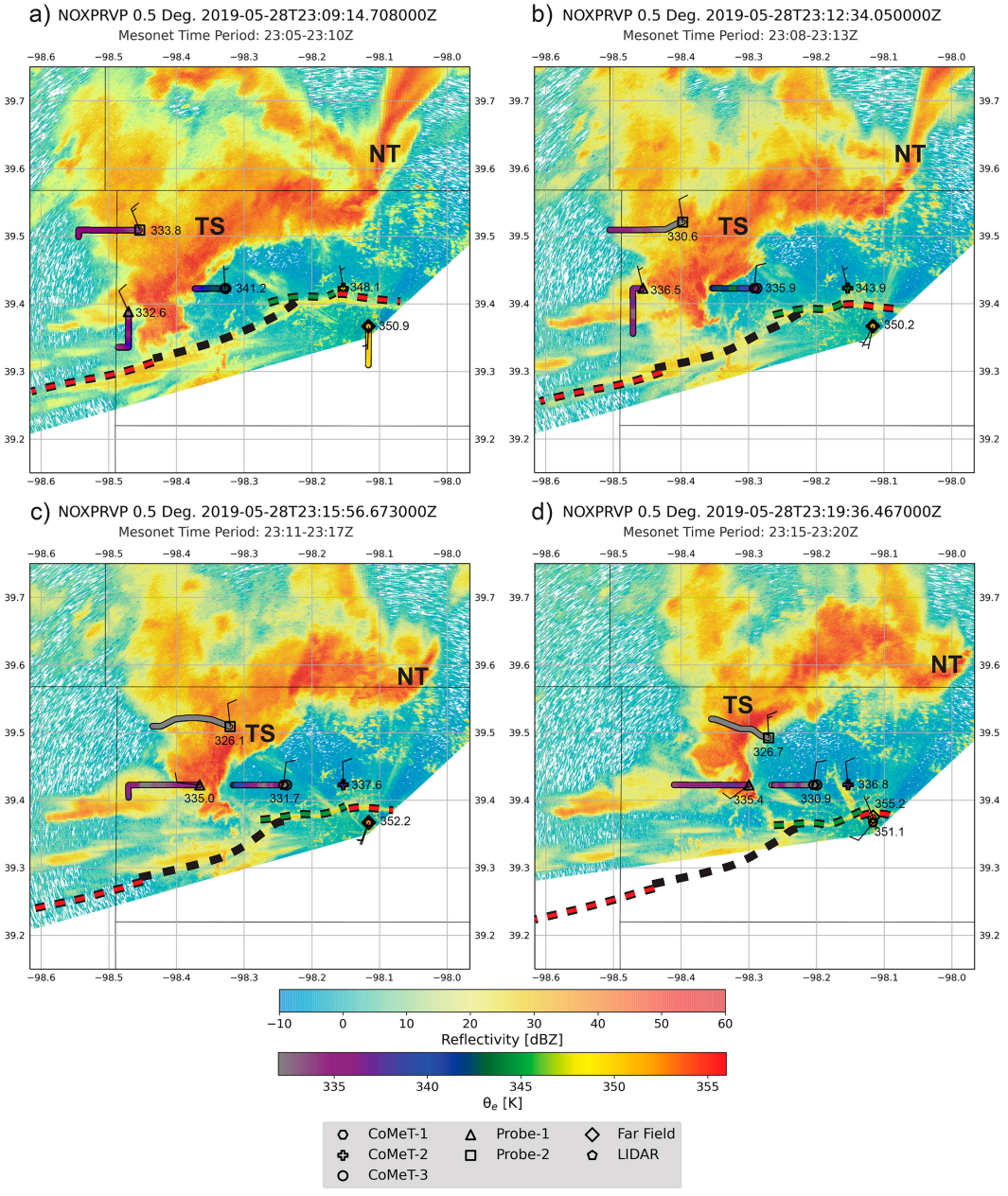

FIG. 21. As in Fig. 17, but between 2309 and 2319 UTC. A green dashed curve is used to demarcate the second (and stronger) outflow boundary (OFB2) from the nontornadic supercell.

By 2250 UTC (Fig. 24a), the Tipton supercell had crossed the section of the front that had been overtaken by the first outflow boundary, OFB1, associated with the nontornadic storm. MAHTE air was possibly still present closer to the Tipton storm on this boundary. The nontornadic storm continued to move farther behind the front into the cooler air mass and maintained a mesocyclone as seen through radial velocity data.

The EF2 tornado track ended around 2302 UTC just south of Tipton, KS (NWS 2021b), possibly because of stable air entering the updraft from the air mass behind OFB1. By 2309 UTC, OFB2 began to undercut the mesocyclone of the Tipton storm (Fig. 21, refer to Fig. 24c for the boundary position relative to the WSR-88D representation of the storm at 2316 UTC). The low-level mesocyclone (exhibited through the radial velocity data) became disorganized after this time. Meanwhile, the nontornadic supercell maintained an organized low-level mesocyclone from 2250 to 2326 UTC (Figs. 24a,c,e) and after the analysis period.

4. Conclusions and discussion

A tornadic supercell interacted with multiple preexisting airmass boundaries on 28 May 2019 in north-central Kansas

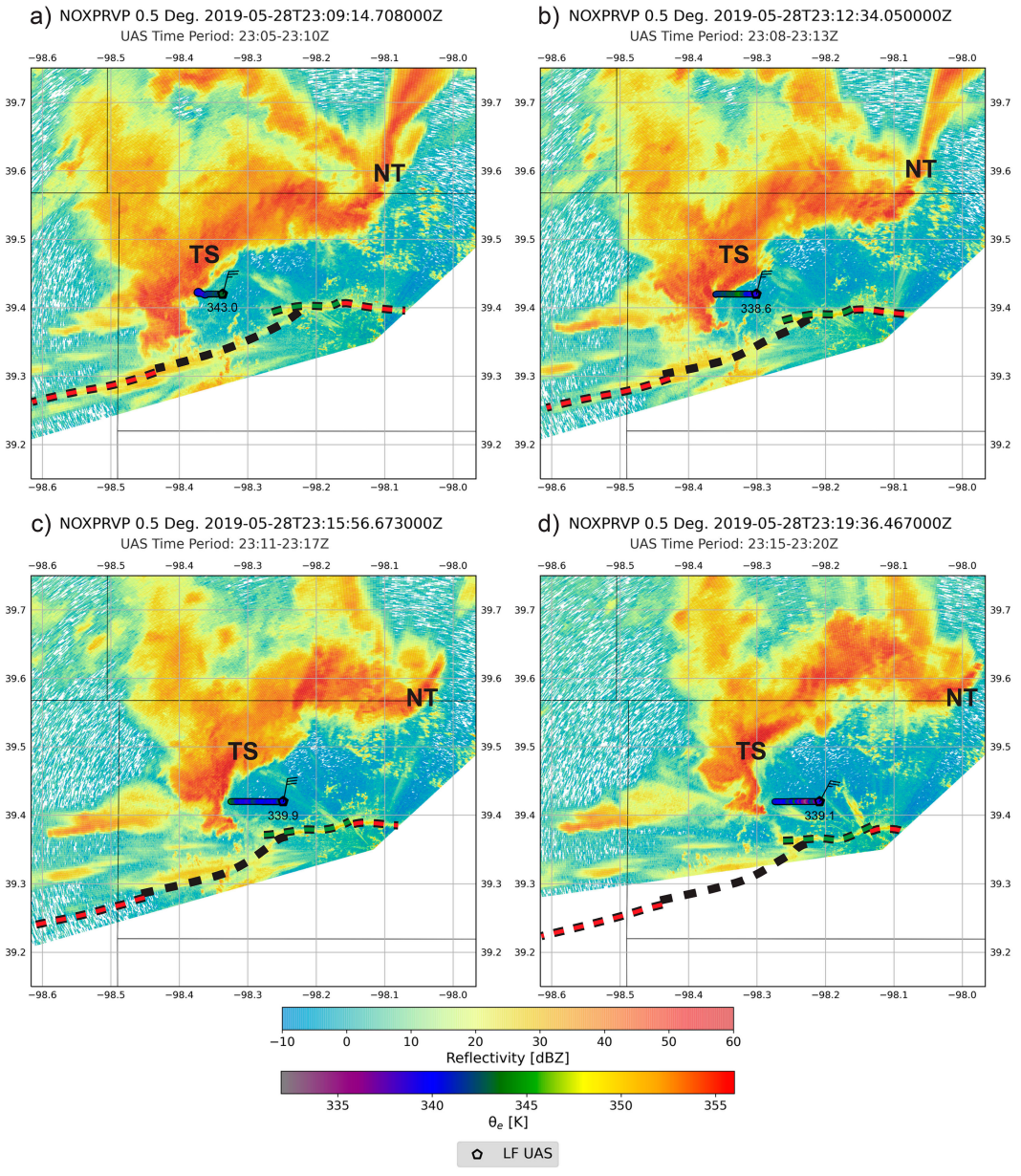

FIG. 22. As in Fig. 18, but between 2309 and 2319 UTC and around 270 m AGL. A green dashed curve is used to demarcate the second (and stronger) outflow boundary (OFB2) from the nontornadic supercell.

and was observed by the 2019 TORUS field campaign. The primary airmass boundary was a synoptic-scale warm front associated with a MAHTE. Data from mobile mesonets, UAS, environmental soundings, mobile radars, *GOES-16* visible satellite imagery, and Kansas mesonet surface stations were used to investigate the characteristics of the MAHTE and examine the front's influence on the tornadic (Tipton) supercell. The MAHTE boundary-normal width and vertical depth were estimated to be ~13 km and ~400 m, respectively. The higher Θ_e in the cooler air mass was characterized by similar instability, greater vertical wind shear, and a lower LCL relative to the warm sector environment providing a relatively small region in which conditions were more favorable for tornadic supercells.

The warm air mass showed signs of stabilization in the shadow of the storm's anvil. The inferred decoupling likely reduced mixing allowing for moisture and Θ_e to increase near the surface, rendering the MAHTE more difficult to distinguish from the warm-side air mass. However, observations above the near-surface inversion still showed a MAHTE was present, underscoring the importance of above-surface observations for characterizing air masses in severe storm environments.

Analysis of the front location showed that the Tipton supercell initiated south of the front potentially just ahead of a cold

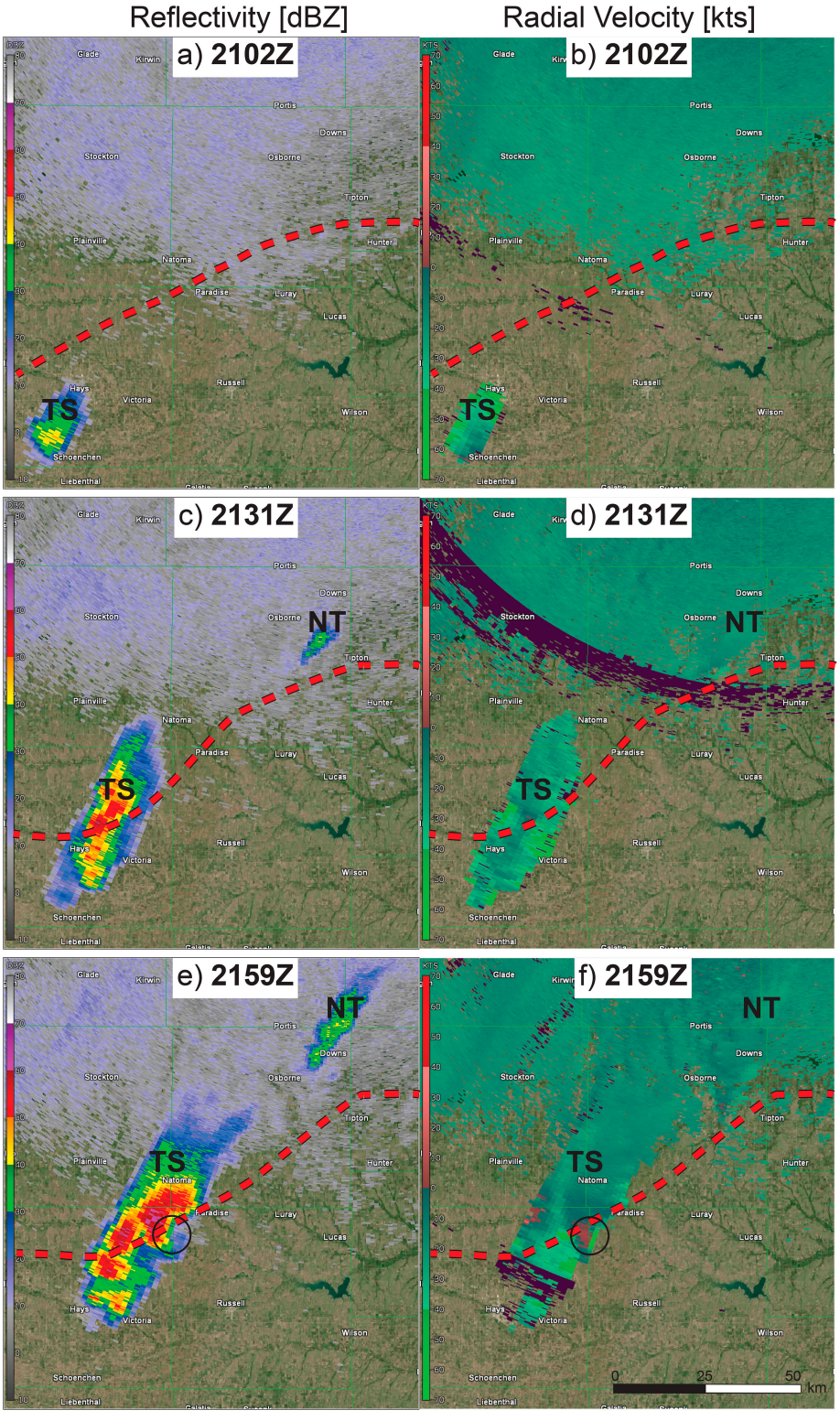

FIG. 23. KUEX WSR-88D 0.5° scans of the base reflectivity and de-aliased radial velocity fields at (a),(b) 2102; (c),(d) 2131; and (e),(f) 2159 UTC 28 May 2019. The red dashed curve represents the front location, TS denotes the Tipton supercell, and NT denotes the nontornadic supercell. In (e) and (f) the black circle highlights the location of the mesocyclone associated with the Tipton supercell based on several scan heights.

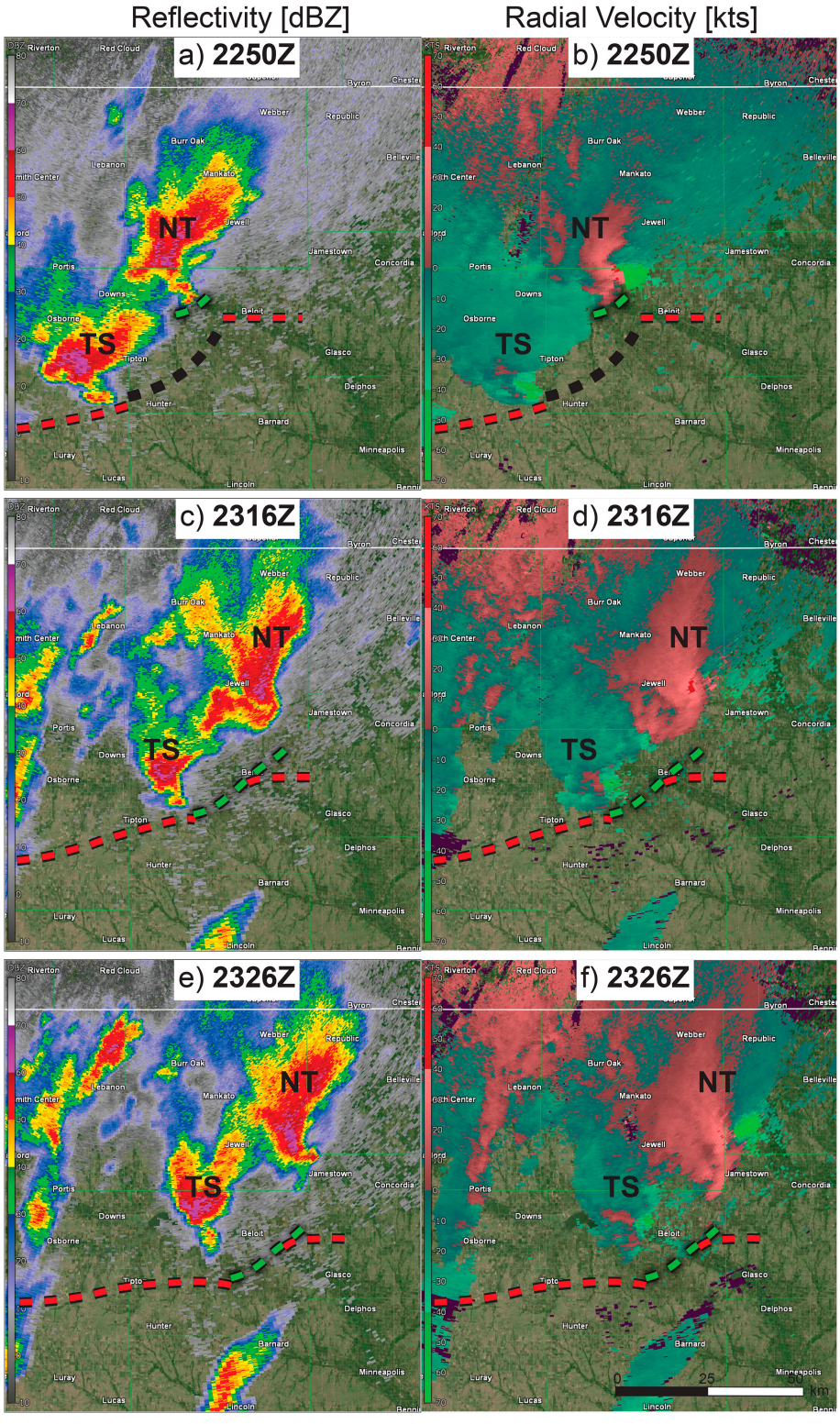

FIG. 24. As in Fig. 23, but at (a),(b) 2250; (c),(d) 2316; and (e),(f) 2326 UTC 28 May 2019. The dashed black (green) curve demarcates OFB1 (OFB2).

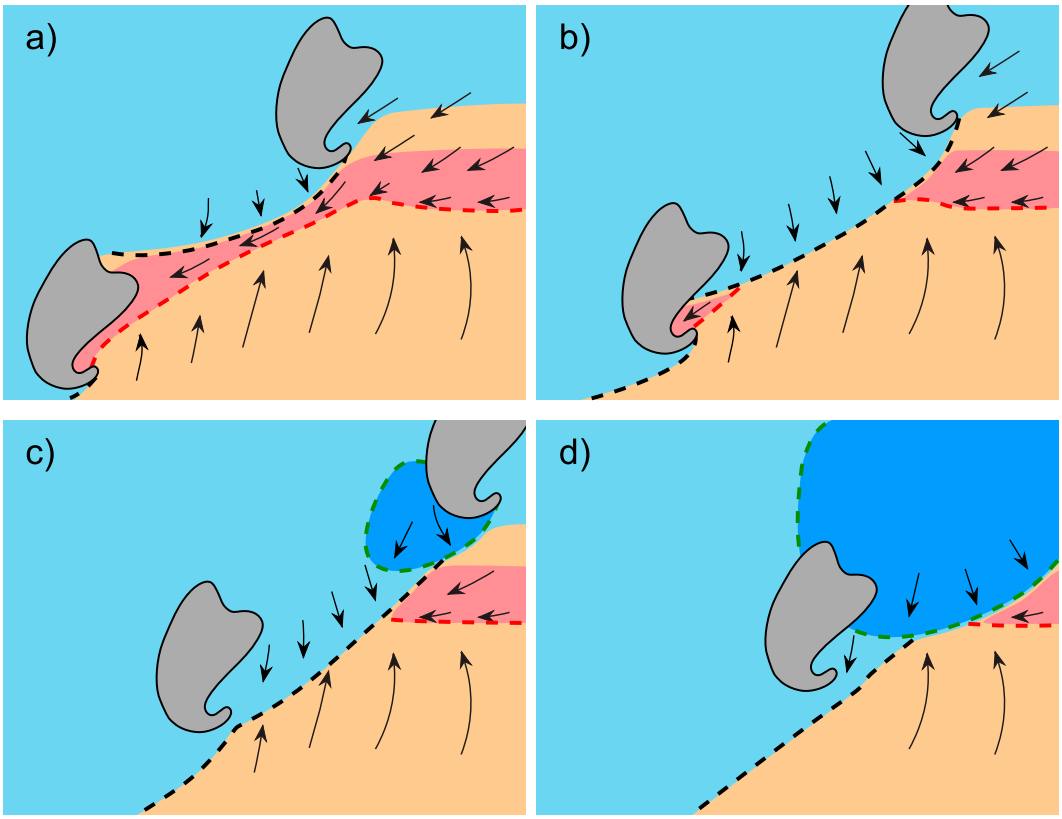

FIG. 25. Conceptual schematic summarizing the evolution of the 28 May 2019 tornadic and nontornadic supercell interactions with the front (red dashed curve) and the two outflow boundaries from the nontornadic supercell (black dashed curve represents the OFB1 and the green dashed curve represents OFB2). The black arrows represent the general flow field within each air mass. The colored regions represent the general airmass characteristics based on Θ_e with red, beige, light blue, and dark blue corresponding to the MAHTE, warm air mass, first outflow air mass, and second outflow air mass, respectively. Two supercells are outlined in black. Note that the more southern (northern) storm represents the Tipton (nontornadic) supercell.

front, moved northeast throughout its lifetime, and approached the front from the warm side. The storm became tornadic as it moved along the boundary suggesting it had intensified and was likely ingesting parcels from the MAHTE.

The evolution of a nontornadic supercell was also investigated as it modified the environment of the tornadic supercell after producing two outflow boundaries. This supercell formed north of the front in the MAHTE and progressed into the cool air throughout its life. The nontornadic supercell then produced a weak outflow boundary that gradually moved southeast and collided with the front replacing the MAHTE with a cooler and drier air mass. This first outflow from the nontornadic supercell began interacting with the Tipton storm around the time the EF2 tornado dissipated (2302 UTC). Around 10 min later, the nontornadic supercell produced a second outflow boundary that pushed a very stable air mass ahead of the Tipton supercell into its inflow region, and this stable air mass likely prevented other tornadoes from forming. Figure 25 provides a conceptual illustration of the interaction of the Tipton storm with the multiple preexisting boundaries.

The primary difference between the tornadic Tipton storm and the nontornadic storm is that the nontornadic supercell formed on the front and moved into the cool air mass early on in its lifetime. While prior work indicates that tornadic supercells can still form or maintain themselves when moving to the cool side of a boundary (Rasmussen et al. 2000; Gilmore and Wicker 2002; Guyer and Ewald 2004; Groenemeijer et al. 2011), the shallow depth and width of the MAHTE likely kept the favorable conditions restricted mostly south of the nontornadic storm.

Residence time is also important when considering where the nontornadic storm formed along the boundary. The nontornadic supercell developed closer to where the front had a more zonal orientation while the Tipton supercell interacted with the front where it had a southwest-to-northeast orientation. Both supercells moved to the northeast meaning the Tipton supercell moved more parallel to the boundary than the nontornadic supercell. Studies have found that supercell tornadogenesis is more likely with supercells that move along boundaries (Atkins et al. 1999; Magee and Davenport 2020). The nontornadic supercell also potentially ingested stable parcels

farther northeast of the MAHTE while the Tipton supercell ingested parcels from both the warm air mass and MAHTE.

Several of the conclusions from this work must be qualified as a result of limited data. It is unknown if the MAHTE actually extended down the length of the front to the Tipton storm. By the time the Tipton storm could have ingested parcels from the MAHTE, environmental changes could have occurred due to the effects of anvil shading or microscale processes not captured in the data or available observational tools. Even if a MAHTE was in place, the exact nature of the interaction of the boundary and MAHTE with the storm is not known. Future work on this case should involve a modeling-based examination of the impact of a similar boundary and MAHTE on simulated storms.

Acknowledgments. Acknowledgements are owed to my advisor Dr. Adam Houston, and my committee members Dr. Matthew Van Den Broeke and Dr. Clint Rowe for guiding me through my masters' research and providing support throughout the duration of this project. I give my thanks to members of the Severe Storms Research Group for providing feedback on my work and many insightful discussions. I also want to acknowledge everyone who participated in TORUS 2019 for collecting the many datasets used in this work. Additional thanks are given to Bobby Jackson, Alex Scheuth, and Elizabeth Venteicher, for contributing to different aspects of my analysis. Finally, I would like to thank my family and friends for their incredible and consistent support throughout this project. This work was made possible through the National Science Foundation Award 1824649 and the Earth and Atmospheric Sciences Department at the University of Nebraska–Lincoln.

Data availability statement. All TORUS datasets are openly available on the NCAR/UCAR Earth Observing Laboratory at https://data.eol.ucar.edu/master_lists/generated/torus_2019/ with the specific datasets used in this work listed in the reference section. The Kansas Mesonet data are openly available at https://mesonet.k-state.edu/weather/historical/, with 5-min observations acquired through contacting the office at kansas-wdl@k-state.edu. *GOES-16* visible satellite imagery is accessible through Amazon Web Services and can be downloaded through https://home.chpc.utah.edu/~u0553130/Brian_Blaylock/cgi-bin/generic_AWS_download.cgi?DATASET=noaa-goes16&BUCKET=ABI-L1b-RadM/2019. The Purdue Windsond data were provided through personal communication with Dr. Daniel Dawson (dandawson@purdue.edu). The Py-ART and PyDDA tools are both available on GitHub repositories at https://github.com/ARM-DOE/pyart and https://github.com/openradar/PyDDA, respectively. GR2Analyst version 2 is available for purchase and can be downloaded at http://grlevelx.com/gr2analyst_2/.

REFERENCES

Atkins, N. T., M. L. Weisman, and L. J. Wicker, 1999: The influence of preexisting boundaries on supercell evolution. *Mon. Wea. Rev.*, **127**, 2910–2927, https://doi.org/10.1175/1520-0493(1999)127<2910:TIOPBO>2.0.CO;2.

Barnes, S. L., 1964: A technique for maximizing details in numerical weather map analysis. *J. Appl. Meteor.*, **3**, 396–409, https://doi.org/10.1175/1520-0450(1964)003<0396:ATFMDI>2.0.CO;2.

Blumberg, W. G., K. T. Halbert, T. A. Supinie, P. T. Marsh, R. L. Thompson, and J. A. Hart, 2017: SHARPpy: An open-source sounding analysis toolkit for the atmospheric sciences. *Bull. Amer. Meteor. Soc.*, **98**, 1625–1636, https://doi.org/10.1175/BAMS-D-15-00309.1.

Burgess, D., T. Mansell, and A. Reinhart, 2020: TORUS_2019: NOXP radar data, version 1.0. UCAR/NCAR–Earth Observing Laboratory, accessed 2 February 2021, https://doi.org/10.26023/BX3D-5PBJ-6P0A.

Davies-Jones, R. P., 1979: Dual-Doppler radar coverage area as a function of measurement accuracy and spatial resolution. *J. Appl. Meteor.*, **18**, 1229–1233, https://doi.org/10.1175/1520-0450-18.9.1229.

Elston, J. S., J. Roadman, M. Stachura, B. Argrow, A. Houston, and E. Frew, 2011: The tempest unmanned aircraft system for in situ observations of tornadic supercells: Design and VORTEX2 flight results. *J. Field Rob.*, **28**, 461–483, https://doi.org/10.1002/rob.20394.

Frame, J., and P. Markowski, 2010: Numerical simulations of radiative cooling beneath the anvils of supercell thunderstorms. *Mon. Wea. Rev.*, **138**, 3024–3047, https://doi.org/10.1175/2010MWR3177.1.

Frew, E., B. Argrow, S. Borenstein, J. Bird, S. Swenson, A. Hirst, M. Rhodes, and C. Choate, 2020: TORUS_2019: University of Colorado RAAVEN sUAS data, version 1.0. Accessed 2 February 2021, https://doi.org/10.26023/FJD8-VMV2-XW0Y.

Gilmore, M. S., and L. J. Wicker, 2002: Influences of the local environment on supercell cloud-to-ground lightning, radar characteristics, and severe weather on 2 June 1995. *Mon. Wea. Rev.*, **130**, 2349–2372, https://doi.org/10.1175/1520-0493(2002)130<2349:IOTLEO>2.0.CO;2.

Groenemeijer, P., U. Corsmeier, and C. Kottmeier, 2011: The development of tornadic storms on the cold side of a front favoured by local enhancement of moisture and CAPE. *Atmos. Res.*, **100**, 765–781, https://doi.org/10.1016/j.atmosres.2010.10.028.

Guyer, J. L., and R. Ewald, 2004: Record hail event—Examination of the Aurora, Nebraska supercell of 22 June 2003. *22nd Conf. on Severe Local Storms*, Hyannis, MA, Amer. Meteor. Soc., 11B.1, https://ams.confex.com/ams/11aram22sls/techprogram/paper_82087.htm.

Hanft, W., and A. L. Houston, 2018: An observational and modeling study of mesoscale air masses with high theta-E. *Mon. Wea. Rev.*, **146**, 2503–2524, https://doi.org/10.1175/MWR-D-17-0389.1.

Helmus, J. J., and S. M. Collis, 2016: The Python ARM Radar Toolkit (Py-ART), a library for working with weather radar data in the Python programming language. *J. Open Res. Software*, **4**, e25, https://doi.org/10.5334/jors.119.

Honda, T., and T. Kawano, 2016: A possible mechanism of tornadogenesis associated with the interaction between a supercell and an outflow boundary without horizontal shear. *J. Atmos. Sci.*, **73**, 1273–1292, https://doi.org/10.1175/JAS-D-14-0347.1.

Houston, A., K. Axon, and A. Erwin, 2020a: TORUS_2019: UNL Combined Mesonet and Tracker (CoMeT-2) mobile mesonet data, version 1.2. UCAR/NCAR–Earth Observing

Laboratory, accessed 2 February 2021, https://doi.org/10.26023/JWPF-089R-8J0B.

——, B. Argrow, M. C. Coniglio, E. W. Frew, E. N. Rasmussen, C. C. Weiss, and C. L. Ziegler, 2020b: Targeted observation by radars and UAS of Supercells (TORUS): Summary of the 2019 field campaign. *Severe Local Storms Symp.*, Boston, MA, Amer. Meteor. Soc., 1.3, https://ams.confex.com/ams/2020Annual/webprogram/Paper369999.html.

——, K. Axon, and A. Erwin, 2021a: TORUS_2019: UNL Combined Mesonet and Tracker (CoMeT-1) mobile mesonet data, version 2.1. UCAR/NCAR–Earth Observing Laboratory, accessed 2 February 2021, https://doi.org/10.26023/B967-JN6J-AY03.

——, ——, and ——, 2021b: TORUS_2019: UNL Combined Mesonet and Tracker (CoMeT-3) mobile mesonet data, version 1.1. UCAR/NCAR–Earth Observing Laboratory, accessed 2 February 2021, https://doi.org/10.26023/DCF0-DW77-H20Q.

Jackson, R., S. Collis, T. Lang, C. Potvin, and T. Munson, 2020: PyDDA: A Pythonic direct data assimilation framework for wind retrievals. *J. Open Res. Software*, **8**, 20, https://doi.org/10.5334/jors.264.

Johns, R. H., C. Broyles, D. Eastlack, H. Guerrero, and K. Harding, 2000: The role of synoptic patterns and temperature and moisture distribution in determining the locations of strong and violent tornado episodes in the north central United States: A preliminary examination. Preprints, *20th Conf. on Severe Local Storms*, Orlando, FL, Amer. Meteor. Soc., 15.2, https://ams.confex.com/ams/Sept2000/webprogram/Paper16415.html.

Kansas State University, 2019: Kansas mesonet: Weather data library—Historical weather. Kansas State University, accessed 15 March 2022, https://mesonet.k-state.edu/weather/historical/.

Laflin, J. M., and A. L. Houston, 2012: A modeling study of supercell development in the presence of a preexisting air-mass boundary. *Electron. J. Severe Storms Meteor.*, **7** (1), https://ejssm.org/archives/wp-content/uploads/2021/09/vol7-1.pdf.

Maddox, R. A., L. R. Hoxit, and C. F. Chappell, 1980: A study of tornadic thunderstorm interactions with thermal boundaries. *Mon. Wea. Rev.*, **108**, 322–336, https://doi.org/10.1175/1520-0493(1980)108<0322:ASOTTI>2.0.CO;2.

Magee, K. M., and C. E. Davenport, 2020: An observational analysis quantifying the distance of supercell-boundary interactions in the Great Plains. *J. Oper. Meteor.*, **8**, 15–38, https://doi.org/10.15191/nwajom.2020.0802.

Markowski, P. M., E. N. Rasmussen, and J. M. Straka, 1998: The occurrence of tornadoes in supercells interacting with boundaries during VORTEX-95. *Wea. Forecasting*, **13**, 852–859, https://doi.org/10.1175/1520-0434(1998)013<0852:TOOTIS>2.0.CO;2.

Miloshevich, L. M., A. Paukkunen, H. Vömel, and S. J. Oltmans, 2004: Development and validation of a time-lag correction for Vaisala radiosonde humidity measurements. *J. Atmos. Oceanic Technol.*, **21**, 1305–1327, https://doi.org/10.1175/1520-0426(2004)021<1305:DAVOAT>2.0.CO;2.

NOAA, 2019: May 28, 2019 0100 UTC day 1 convective outlook. Accessed 12 November 2022, https://www.spc.noaa.gov/products/outlook/archive/2019/day1otlk_20190528_0100.html.

Nowotarski, C. J., and P. M. Markowski, 2016: Modifications to the near-storm environment induced by simulated supercell thunderstorms. *Mon. Wea. Rev.*, **144**, 273–293, https://doi.org/10.1175/MWR-D-15-0247.1.

NWS, 2021a: National Weather Service Birmingham AL reduced tornado warning false alarm rate by 31% since April 2011. Accessed 2 December 2021, https://www.weather.gov/bmx/research_falsealarms.

——, 2021b: May 26–28, 2019: Tornadoes on 3-consecutive days! (including an EF-2 in KS). Accessed 2 December 2021, https://www.weather.gov/gid/latemay2019tors.

Pauley, P. M., and X. Wu, 1990: The theoretical, discrete, and actual response of the Barnes objective analysis scheme for one- and two-dimensional fields. *Mon. Wea. Rev.*, **118**, 1145–1164, https://doi.org/10.1175/1520-0493(1990)118<1145:TTDAAR>2.0.CO;2.

Plymouth State Weather Center, 2022: Contoured constant pressure level/whole sounding data upper air maps from archived data. Plymouth State University, accessed 20 November 2022, https://vortex.plymouth.edu/myowxp/upa/ctrmap-a.html.

Potvin, C. K., A. Shapiro, and M. Xue, 2012: Impact of a vertical vorticity constraint in variational dual-Doppler wind analysis: Tests with real and simulated supercell data. *J. Atmos. Oceanic Technol.*, **29**, 32–49, https://doi.org/10.1175/JTECH-D-11-00019.1.

Rasmussen, E. N., S. Richardson, J. M. Straka, P. M. Markowski, and D. O. Blanchard, 2000: The association of significant tornadoes with a baroclinic boundary on 2 June 1995. *Mon. Wea. Rev.*, **128**, 174–191, https://doi.org/10.1175/1520-0493(2000)128<0174:TAOSTW>2.0.CO;2.

Shapiro, A., C. K. Potvin, and J. Gao, 2009: Use of a vertical vorticity equation in variational dual-Doppler wind analysis. *J. Atmos. Oceanic Technol.*, **26**, 2089–2106, https://doi.org/10.1175/2009JTECHA1256.1.

Smith, E., and M. Coniglio, 2019: TORUS 2019:NSSL mobile Lidar data, version 1.0. UCAR/NCAR–Earth Observing Laboratory, accessed 2 February 2021, https://doi.org/10.26023/EVYG-3VV6-YC0E.

SPC, 2022a: Prototype interactive local storm reports display. Accessed 20 November 2022, https://www.spc.noaa.gov/exper/reports/.

——, 2022b: Storm prediction center product & report archives. Accessed 20 November 2022, https://www.spc.noaa.gov/archive/.

Thompson, R. L., R. Edwards, J. A. Hart, K. L. Elmore, and P. Markowski, 2003: Close proximity soundings within supercell environments obtained from the rapid update cycle. *Wea. Forecasting*, **18**, 1243–1261, https://doi.org/10.1175/1520-0434(2003)018<1243:CPSWSE>2.0.CO;2.

van Den Kroonenberg, A., T. Martin, M. Buschmann, J. Bange, and P. Vörsmann, 2008: Measuring the wind vector using the autonomous mini aerial vehicle M^2AV. *J. Atmos. Oceanic Technol.*, **25**, 1969–1982, https://doi.org/10.1175/2008JTECHA1114.1.

Waugh, S., 2020a: TORUS_2019: NSSL mobile mesonet data, version 1.1. UCAR/NCAR–Earth Observing Laboratory, accessed 2 February 2021, https://doi.org/10.26023/2Y87-XEEB-7W13.

——, 2020b: TORUS_2019: NSSL Mobile Quality Controlled (QC) radiosonde data, version 1.0. UCAR/NCAR–Earth Observing Laboratory, accessed 2 February 2021, https://doi.org/10.26023/MDEM-SG4J-5P10.

Weiss, C., and A. Schueth, 2019: TORUS_2019: Texas Tech University Ka Band (TTUKA) mobile radar data, version 1.2. UCAR/NCAR–Earth Observing Laboratory, accessed 2 February 2021, https://doi.org/10.26023/9QY1-9TWD-TB08.

Wildmann, N., S. Ravi, and J. Bange, 2014: Towards higher accuracy and better frequency response with standard multi-hole probes in turbulence measurement with Remotely Piloted Aircraft (RPA). *Atmos. Meas. Tech.*, **7**, 1027–1041, https://doi.org/10.5194/amt-7-1027-2014.

WPC, 2022: Surface analysis 18Z Tue May 28 2019. Accessed 20 November 2022, https://www.wpc.ncep.noaa.gov/html/sfc-zoom.php.